AFRL-AFOSR-VA-TR-2019-0128

Passive and Active Patterned Roughness for Cross-flow Transition Control at Mach 6

Thomas Corke
UNIVERSITY OF NOTRE DAME DU LAC

05/03/2019
Final Report

Air Force Research Laboratory
AF Office Of Scientific Research (AFOSR)/ RTA1
Arlington, Virginia 22203
Air Force Materiel Command

DISTRIBUTION A: Distribution approved for public release.

REPORT DOCUMENTATION PAGE

Form Approved
OMB No. 0704-0188

1. REPORT DATE *(DD-MM-YYYY)*	2. REPORT TYPE	3. DATES COVERED *(From - To)*
06-05-2019	Final Performance	01 Aug 2015 to 31 Jan 2019

4. TITLE AND SUBTITLE
Passive and Active Patterned Roughness for Cross-flow Transition Control at Mach 6

5a. CONTRACT NUMBER

5b. GRANT NUMBER
FA9550-15-1-0278

5c. PROGRAM ELEMENT NUMBER
61102F

6. AUTHOR(S)
Thomas Corke, Eric Matlis

5d. PROJECT NUMBER

5e. TASK NUMBER

5f. WORK UNIT NUMBER

7. PERFORMING ORGANIZATION NAME(S) AND ADDRESS(ES)
UNIVERSITY OF NOTRE DAME DU LAC
940 GRACE HALL
NOTRE DAME, IN 465565602 US

8. PERFORMING ORGANIZATION REPORT NUMBER

9. SPONSORING/MONITORING AGENCY NAME(S) AND ADDRESS(ES)
AF Office of Scientific Research
875 N. Randolph St. Room 3112
Arlington, VA 22203

10. SPONSOR/MONITOR'S ACRONYM(S)
AFRL/AFOSR RTA1

11. SPONSOR/MONITOR'S REPORT NUMBER(S)
AFRL-AFOSR-VA-TR-2019-0128

12. DISTRIBUTION/AVAILABILITY STATEMENT
A DISTRIBUTION UNLIMITED: PB Public Release

13. SUPPLEMENTARY NOTES

14. ABSTRACT
The program was designed investigate passive and active (plasma) patterned roughness for transition control on a sharp right-circular cone at an angle of attack at Mach 6.0. A cone angle of attack of 6deg. was set to produce a mean cross-flow velocity component in the boundary layer over the cone by which the cross-flow instability was the dominant mechanism of turbulent transition. The approach to transition control was based on exciting less-amplified (subcritical) stationary cross-flow modes that suppress the growth of the more-amplified (critical) cross-flow modes, and thereby delay transition. The passive roughness consisted of an azimuthal array of indentations (dimples) at an axial location that is just upstream of the first linear stability neutral growth branch for cross-flow modes. Two roughness azimuthal wavenumbers were examined: one that was in the band of most amplified stationary cross-flow modes, representing the ``critical' roughness condition; and the second being at a 1.5-times higher azimuthal wavenumber that represented the ``subcritical' roughness condition intended to suppress transition. In subsequent experiments a plasma actuator on the cone surface, just downstream of the roughness array, was used to produce a disturbance at the most amplified traveling cross-flow mode frequency. The purpose was to investigate under controlled conditions, a nonlinear (quadratic) interaction between the stationary and traveling cross-flow modes that could affect the transition location. The experiments were performed in the Air Force Academy Mach 6.0 Ludwieg Tube Facility, that is not designed to produce ``quiet' flow. Under these conditions, the subcritical wave number roughness increased the transition Reynolds number by 25%. This was less than the 40% obtained with the same model and roughness in a ``quiet' Mach 3.5 tunnel. The experiments also revealed evi

15. SUBJECT TERMS
Transition control, Roughness element, Active (plasma) patterned roughness

16. SECURITY CLASSIFICATION OF:			17. LIMITATION OF ABSTRACT	18. NUMBER OF PAGES	19a. NAME OF RESPONSIBLE PERSON
a. REPORT	b. ABSTRACT	c. THIS PAGE			LEYVA, IVETT
Unclassified	Unclassified	Unclassified	UU		19b. TELEPHONE NUMBER *(Include area code)* 703-696-8478

To: technicalreports@afosr.af.mil

Subject: Final Progress Statement to Dr. Ivett Leyva

Contract/Grant Title: Passive and Active Patterned Roughness for Cross-flow Transition Control at Mach 6

Principle Investigator: Thomas C. Corke, University of Notre Dame

Contract/Grant Title: Passive and Active Patterned Roughness for Cross-flow Transition Control at Mach 6

Contract/Grant No.: FA9550-15-1-0278

Reporting Period: August 1, 2015 to April 30, 2019

Final Accomplishments Summary: The program was designed investigate passive and active (plasma) patterned roughness for transition control on a sharp right-circular cone at an angle of attack at Mach 6.0. A cone angle of attack of 6° was set to produce a mean cross-flow velocity component in the boundary layer over the cone by which the cross-flow instability was the dominant mechanism of turbulent transition. The approach to transition control was based on exciting less-amplified (subcritical) stationary cross-flow modes that suppress the growth of the more-amplified (critical) cross-flow modes, and thereby delay transition. The passive roughness consisted of an azimuthal array of indentations (dimples) at an axial location that is just upstream of the first linear stability neutral growth branch for cross-flow modes. Two roughness azimuthal wavenumbers were examined: one that was in the band of most amplified stationary cross-flow modes, representing the "critical" roughness condition; and the second being at a 1.5-times higher azimuthal wavenumber that represented the "subcritical" roughness condition intended to suppress transition. In subsequent experiments a plasma actuator on the cone surface, just downstream of the roughness array, was used to produce a disturbance at the most amplified traveling cross-flow mode frequency. The purpose was to investigate under controlled conditions, a nonlinear (quadratic) interaction between the stationary and traveling cross-flow modes that could affect the transition location. The experiments were performed in the Air Force Academy (AFA) Mach 6.0 Ludwieg Tube Facility, that is not designed to produce "quiet" flow. Under these conditions, the subcritical wavenumber roughness increased the transition Reynolds number by 25%. This

was less than the 40% obtained with the same model and roughnessSchuele et al. [2013] in a "quiet" Mach 3.5 tunnel. The experiments also revealed evidence of a quadratic, sum and difference interaction, between stationary and traveling cross-flow modes that might indicate a mechanism of early transition in conventional (noisy) hypersonic wind tunnels. This was explored with the addition of the plasma actuator. The excitation at the most amplified traveling mode frequency in conjunction with the critical wavenumber roughness, was found to move the transition location upstream by 9%. Cross-bicoherence analysis confirmed the perfect wavenumber matching between the prescribed stationary and traveling modes, leading to the generation of traveling modes at sum and difference wavenumbers. The analysis also documented an interaction between the roughness harmonic wavenumber and the excited primary traveling cross-flow mode to produced a traveling mode at the critical roughness wavenumber. Such interactions between stationary modes generated by surface roughness, and traveling modes generated by free-stream disturbaces, indicates a mechanism for transition in "noisy" environments that can explain the differences in the transition location, and the ability of transition control, between noisy and quiet environments.

Contents

1 Introduction

Interest in flight at hypersonic speeds has led to renewed research efforts on laminar boundary layer transition in hypersonic flows. Besides the interest in fundamental mechanisms, the prediction and control of hypersonic boundary layer transition has a practical importance to surface heating, which increases significantly when the boundary layer becomes turbulent.

Turbulence transition on hypersonic **lifting** bodies is likely to be dominated by a mean cross-flow velocity component that is subject to a cross-flow instability. The first stage of cross-flow instability dominated transition starts with the process of receptivity[Morkovin, 1990a,b, Reshotko, 09-12 June 2008, Saric et al., 2002]. Based on linear stability theory, traveling cross-flow modes are more amplified than stationary cross-flow modes. However, the stationary modes are highly receptive to surface roughness which can provide higher initial amplitudes that compensate for their lower amplification rate. As a result, except in instances of higher free-stream turbulence levels[Bippes, 1999], the stationary modes are the leading mechanism in cross-flow dominated transition. As stationary cross-flow modes grow in amplitude, they form co-rotating vortices. As a result of their approximate alignment with the inviscid streamlines of the baseline flow, the vortices have a strong integrated effect on the boundary layer. As they reach larger amplitudes, they produce a mean flow distortion that includes the formation of an inflected mean velocity profile[Malik et al., 1994, 1999, Chernoray et al., 2005, White and Saric, 2005]. The inflectional velocity profile leads to a secondary inviscid instability that generates small-scale velocity fluctuations and eventually turbulence. These stages of development of the cross-flow instability are presented in comprehensive reviews. Saric et al. [2003], Reed and Saric [1989], Wassermann and Kloker [2002] and Bonfigli and Kloker [2007].

Experimental efforts on hypersonic cross-flow transition have largely focused on generic shapes such as right-circular cones at an angle of attack, and elliptic cones. The conical flow at incidence generates a streamline-normal pressure gradient which, if properly designed, can lead to a mean cross-flow. Recent experiments by Craig and Saric [2016] on a right-circular cone at an angle of attack at Mach 6 indicated that the growth and development of stationary and traveling cross-flow modes was largely consistent with that observed in low-speed experiments. However following amplitude saturation, the secondary instability development was slower. This difference can ultimately impact transition, and transition control which is almost completely based on low Mach number experiments.

The approach to control cross-flow dominated transition stems from the extreme receptivity of the instability to surface roughness. This feature was exploited by Corke and Knasiak [1998a] and Corke et al. [2007] to excite selected wavenumbers of cross-flow modes in the boundary layer over a rotating disk, which is a canonical three-dimensional flow that exemplifies the cross-flow instability.

Saric et al. [1998] and Radeztsky Jr. et al. [1999] exploited this property in their swept wing experiments to excite fixed spanwise wavenumber stationary cross-flow modes using arrays of micron-sized circular distributed roughness elements. They demonstrated that stationary cross-flow modes at the forced spanwise wavenumber exclusively appeared in the boundary layer. Super-harmonic wavenumbers of the forced wavenumber were also possible

to appear, however lower wavenumbers were always completely suppressed.

These observations led to the concept of exciting less amplified stationary cross-flow modes as a means of controlling transition to turbulence in these flows. The key element was that the spanwise wavenumber of the forced mode had to be higher than those of the naturally amplified band. This would guarantee that no disturbance energy would cascade through nonlinear interactions to lower, more-amplified wavenumbers. Saric et al. [1998] referred to this approach of cross-flow transition control as "subcritical forcing". This was in reference to the band of initially amplified spanwise wavenumbers being the "critical" wavenumbers. Forcing of that amplified band of wavenumbers is then referred to as "critical forcing".

Transition control comes by biasing the natural selection mechanism by raising the initial amplitude of the less-amplified cross-flow mode at the subcritical wavenumber, so that it initially dominates the instability growth process. The growth of the forced mode inhibits the growth of the more amplified (critical wavenumber) stationary mode by modifying the basic state. Ultimately the forced mode decays and the flow eventually becomes turbulent. However, in swept wing experiments[Radeztsky Jr. et al., 1999, Saric et al., 1998, Saric and Reed, 2002], the approach has been shown to produce a substantial increase in the transition Reynolds number.

A majority of the experiments on cross-flow dominated transition to turbulence have been performed on swept wings at low, subsonic Mach number. In such experiments[Saric et al., 1998] patterned surface roughness in the form of hemispherical "dots" with a height of 50 μm, was found to provided an effective transition delay. The effect of distributed roughness on swept wings at supersonic Mach numbers was investigated by Saric and Reed [2002], Saric et al. [2004], Semionov and Kosinov [2007] and Semionov et al. [2006].

There have been a number of cross-flow transition experiments at supersonic Mach numbers. These have primarily been on right-circular cones at angles of attack. These include experiments by King [1992] at Mach 3.5, and by Wolf and Laub [1997] at Mach 1.6. Both of these studies were concerned with correlating transition data between wind tunnel and free-flight experiments. However, King [1992] was the first to mention the cross-flow instability as a transition mechanism.

In general, the cross-flow instability growth rate is a maximum where the cross-flow Reynolds number is a maximum. The cross-flow Reynolds number is defined as $Re_{CF} = V_{max}\delta/\nu$, where V_{max} is the maximum cross-flow velocity, normal to the edge inviscid streamline. For a cone at an angle of attack, the cross-flow Reynolds number increases and then decreases from the windward side of the cone to the leeward side. The maximum occurs towards an azimuthal location, $\theta \simeq 130^\circ$, where $\theta = 0^\circ$ is the windward most ray on the cone, and $\theta = 180^\circ$ is the leeward most ray.

The recent experiment by Schuele et al. [2013] was the first to investigate passive and active patterned roughness for transition control on a sharp-tipped right-circular cone at an angle of attack in a supersonic flow. The model consisted of a 14° right-circular cone placed at a 4.2° angle of attack. This gave a ratio of the angle of attack to half cone angle of $\alpha/\phi_c = 0.6$ in which the cross-flow instability was the dominant mechanism of transition. The experiments were performed in the Mach 3.5 Supersonic Low Disturbance Tunnel (SLDT) at

NASA Langley Research Center that is specially designed to minimize acoustic disturbances.

The cone model had removable tips with different discrete roughness configurations. The passive roughness consisted of indentations (dimples) that were evenly spaced around the cone at an axial location that was just upstream of the first linear stability neutral growth branch for cross-flow modes. The active roughness consisted of an azimuthal array of micron-sized plasma actuators that were designed to produce the effect of passive surface bumps. Two roughness azimuthal wavenumbers were examined: one that was in the band of most amplified stationary cross-flow modes, representing the "critical" roughness condition; and the second being at a 1.5-times higher azimuthal wavenumber that represented the "subcritical" roughness condition intended to suppress transition.

The results showed that the stationary cross-flow modes were receptive to the patterned roughness. Transition front measurements using the Preston tube approach indicated that the transition Reynolds number had increased by 35% with the subcritical wavenumber roughness compared to a baseline smooth tip, and by 40% compared to the critical wavenumber roughness.

Given this background, the objective of the research program was to extend the work of Schuele et al. [2013] into the hypersonic regime to determine if cross-flow dominated turbulent transition could be suppressed with an appropriately patterned discrete roughness. The experiment would be conducted at Mach 6. However contrary to the previous experiment[Schuele et al., 2013], the wind tunnel would be of a conventional (non-quiet) design. Thus, the experiments would examine both the effect of a higher Mach number and the receptivity of the stationary cross-flow modes to the discrete roughness under a higher freestream disturbance condition. The cone model would be the same as in the previous experiment, but placed at an angle of attack that would allow the same roughness cone tips (azimuthal wavenumber and streamwise location) to be used, therefore allowing a direct comparison to the experiments at the lower Mach number. A pair of high bandwidth total pressure probes mounted on a 3-D traversing mechanism would be used to document the boundary layer. The probe frequency response would be sufficient to measure pressure fluctuations associated with the traveling cross-flow modes. Azimuthal profiles of the time-averaged total pressure would be used to document the mean flow distortion produced by the stationary cross-flow modes. The axial development of the mean flow would be used to determine the transition locations for the critical and subcritical patterned roughness. Time-resolved pressure fluctuations would be analyzed to document the spatial development of the traveling cross-flow modes. In addition, the analysis would seek evidence of a nonlinear interaction between the stationary and traveling cross-flow modes that has been documented in the boundary layer on a rotating disk[Corke and Knasiak, 1998a, Corke et al., 2007], which is a canonical three-dimensional flow that exemplifies the cross-flow instability.

2 Experimental Setup

The experiments were conducted in the Air Force Academy (AFA) Mach 6.0 Ludwieg Tube Facility. The facility is based on the design used in the Technical University at Braunschweig, Germany[Estorf et al., 2004]. A schematic of the facility is shown in Figure 1. It consists of a

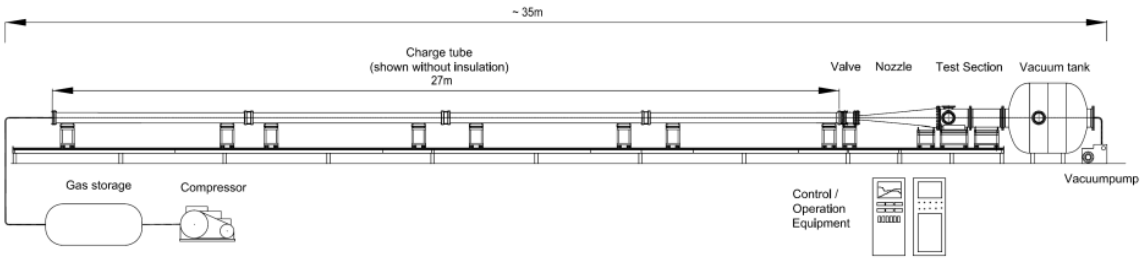

Figure 1: Schematic of U.S. Air Force Academy Mach 6 Ludwieg Tube where the experiments were performed.

27 m long charge tube that is heated and insulated. The pressurized tube discharges through a converging-diverging nozzle from which a Mach 6 flow exits into an open-jet test section. A fast-acting plunger valve is located just upstream of the nozzle throat. When the valve opens, an unsteady expansion wave travels both upstream and downstream. The upstream moving expansion wave reflects at the end of the charge tube and then travels downstream until it reaches the nozzle. The time for this sets the duration of quasi-steady flow conditions in the nozzle and the hypersonic test section. At the conditions of the experiment needed to produce a unit Reynolds number of 10×10^6 m^{-1}, the run time was approximately 80 ms. Further details of the facility are given by Cummings and McLaughlin [2012].

The inside diameter of the test section is 0.5 m, and its length is 0.98 m. For optical access, it has three 0.26 m flanged windows, two on opposite sides, and one on top. Measurements in the test section of the sister facility[Estorf et al., 2004] confirmed a non-uniformity of the Pitot pressure in the core flow of about $\pm 1.2\%$, corresponding to Mach number variations of $\pm 0.6\%$. This non-uniformity results from the narrow wake of the upstream fast-acting valve. To avoid this, the cone model was offset from the centerline of the test section.

The model in the experiment was the same as that used by Schuele et al. [2013]. It is a hollow, thin-walled right-circular cone with a half angle of $\phi_c = 7°$. The total length of the cone is 35.56 cm (14 in). The first 4.303 cm (1.694 in) (tip) of the cone is removable. The base of the cone mounted to a hollow sting that was connected to a vertical strut. The vertical strut bolted to a base plate that attached to the wind tunnel wall, bridging the joint between the test section and the downstream diffuser section. An angled shim under the base plate was used to orient the cone at the $\alpha = 6°$ angle of attack. This gave an $\alpha/\phi_c = 0.86$, which was in the range of dimensionless angles where King [1992] had documented stationary cross-flow vortices.

A schematic of the cone, support sting and 3-D traversing mechanism that mounted on the support sting is shown in Figure 2(a). A photograph of the cone in the wind tunnel test section is shown in Figure 2(b). The wedge-shaped tip of the traversing mechanism that held a pair of high bandwidth total pressure probes is visible near the base of the cone.

The traversing mechanism moved a pair of total-pressure Pitot probes in the wall-normal, axial and azimuthal directions under computer control. Details of the traversing system are given by Schuele [2011]. The motion resolution in the axial direction was 0.1 mm. The

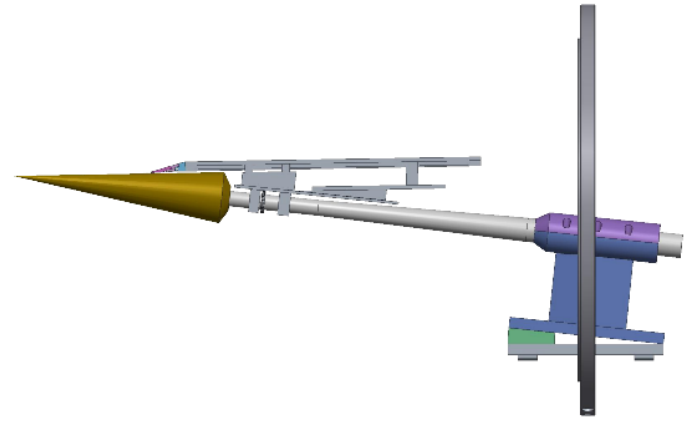

(a)

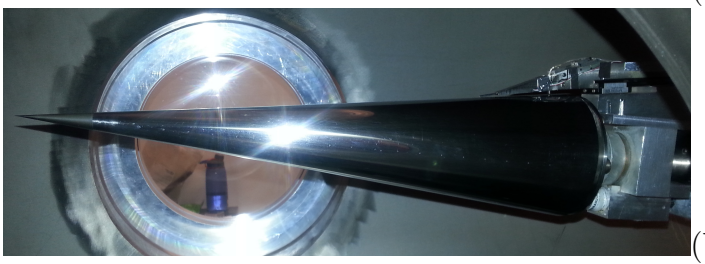

(b)

Figure 2: Schematic of cone model, sting and traversing mechanism and support base holding the model at a 6° angle of attack (a), and photograph of the cone model inside of the test section.

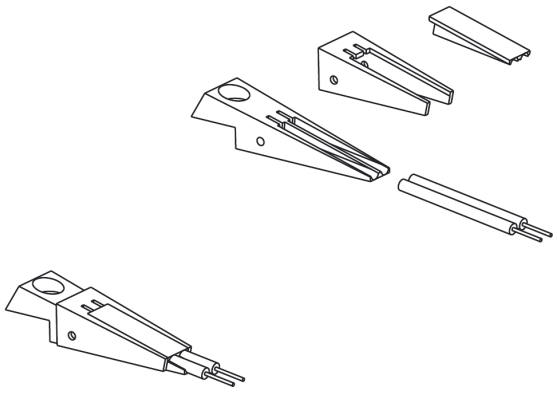

Figure 3: Schematic drawing showing assembly of dual high bandwidth total pressure probe.

resolution in the azimuthal direction was 0.035°, which was 228-times smaller than the the "critical" mode azimuthal wavelength, and 152-times smaller than that of the "subcritical" mode. An optical angle encoder provided feedback to the azimuthal positioning. The resolution in the wall-normal direction was 28μm. This utilized miniature LVDT to provide motion feedback.

The pair of total pressure Pitot probes utilized Kulite model XCE-062-1.7A (1.7 bar, 25 psi absolute) pressure transducers that were mounted in the wedge tip of the traversing mechanism arm. A schematic of the wedge tip assembly is shown in Figure 3. The outside diameter of the Kulite transducers was 1.59 mm. Each transducer was inserted into a circular sleeve whose inside diameter closely matched the outside diameter of the transducer body, and covered the diaphragm end of the pressure transducers. A series of three telescoping hypodermic tubes were then attached to the diaphragm end of the cylindrical sleeve. The hypodermic tubes stepped the outside diameter from 1.72 mm to 0.81 mm, and gave a final inside diameter of 0.43 mm., which was then the sensing diameter of the Pitot probes. This corresponded to 20% of the "critical" mode azimuthal wavelength, and 30% of the "subcritical" mode azimuthal wavelength measured at the middle axial location (12.7 cm) where measurements were performed. The total length of the hypodermic tube assembly was 12.5 mm., which was the same used by Schuele et al. [2013].

Experiments were performed to determine the frequency response of the Pitot probes. This was accomplished using a sound pressure source with a microphone as a reference. The measured response is shown as the dotted curve in Figure 4. This indicates a maximum frequency response, within ±2dB, of approximately 3.5 kHz. This response was too low to capture the traveling cross-flow modes which based on Li et al. [2010] for the conditions of the experiment would be centered about a frequency of 35 kHz. Therefore the output of the Kulite transducers in the Pitot probes was passed through an analog frequency compensation circuit of our design. The response of the compensation circuit alone is shown by the dashed curve in Figure 4. The final response of the frequency compensated Pitot probes is shown by the solid curve in Figure 4. The horizontal red dashed lines mark the ±2dB range. Within this, the compensated Pitot probes have a frequency response of approximately 50 kHz, which

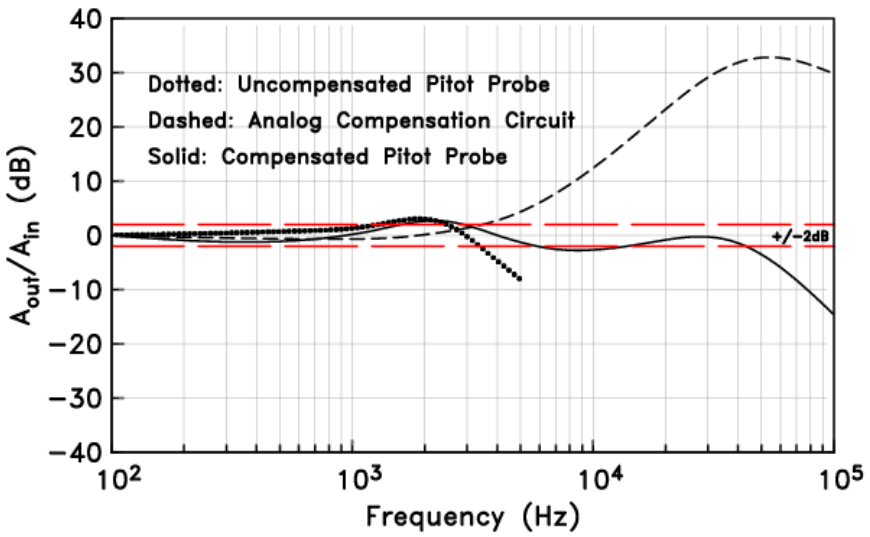

Figure 4: Frequency response of the uncompensated Pitot probes, the analog frequency compensation circuit, and the final frequency compensated Pitot probes.

is sufficient to capture the traveling cross-flow modes. The time series sampling frequency was 100 kHz.

A critical part of the experiment was the design of the roughness tip, specifically the azimuthal wavenumber of the "critical" and "subcritical" roughness, and the axial location for the roughness. The decision drew on experiments at Mach 6 on a 14° right-circular cone at a 6° angle of attack by Swanson and Schneider [2010], and at a close 5.6° angle of attack by Craig and Saric [2016]. Both of these experiments were in quiet tunnels. It also drew on the stability analysis for the conditions of the Swanson and Schneider [2010] experiments that was performed by Li et al. [2010]. These indicated that the band of most amplified stationary cross-flow modes was centered near an azimuthal wavenumber of $m = 45$. This was then chosen to be the "critical" wavenumber. Based on Saric et al. [1998], the "subcritical" wavenumber to be excited for control of the stationary cross-flow mode would then be 1.5-times higher or $m = 68$.

With regard to the axial location of the roughness, information was taken from the analysis of Li et al. [2010] for a unit Reynolds number of 10×10^6 m^{-1}. This is shown in Figure 5. The streamwise location of the roughness array is determined by taking into account Branch I (N=0) of the linear stability neutral curve for stationary cross-flow modes, as well as the theoretical vortex lines. Placing the roughness array too far upstream of Branch I would allow the controlled disturbances to decay, potentially below the background disturbance level. Placing the roughness too far downstream could allow cross-flow modes excited by random roughness or free-stream disturbances to grow to large enough amplitudes that minimize the effect of the roughness array. An equally important consideration on the placement of the roughness are the theoretical vortex lines, along which the disturbances generated by the roughness convects. To be effective, the axial location of the roughness

array needs to intersect with the vortex lines that lead to the region where the linear theory N-factor curve reaches furthest upstream on the cone, indicating the most likely region where turbulent transition is expected to occur. For the cone at a 6° angle of attack, this occurs in the azimuthal region on the lee side between 110° and 150° (where 0° is the windward stagnation line). Based on these two factors, the discrete roughness arrays were located $x_r = 1.27$ cm from the tip of the cone. This happens to be the same axial location of the roughness as used by Schuele et al. [2013], although at a different angle of attack and Mach number. As a result, the same roughness tips and design were utilized in the present experiment.

The removable cone tips were machined from Torlon (Polyamide-Imide (PAI)), which is a relatively hard polymer that can be polished. Following Schuele et al. [2013], the surface roughness patterns consisted of "dimples" that were produced by plunging a conical pin into the surface of the tip. An example of the dimple roughness is shown in Figure 6. This corresponds to the $m = 68$ "subcritical" azimuthal wavenumber. The dimple diameter was approximately 80μm, and the ratio of the diameter to dimple centerline spacing was $d/\lambda \simeq 0.6$. For the $m = 45$ "critical" azimuthal wavenumber, the dimple diameter was approximately 145μm, and the ratio $d/\lambda = 0.65$. In both roughness cases, the spacing between dimples satisfied the discrete roughness criteria[Saric, 2008] that $d/\lambda \geq 0.5$.

The depth of the dimple holes was based on the extent that the conical pin was inserted into the surface to achieve the required dimple diameter. For the larger diameter dimples for the $m = 45$ "critical" azimuthal wavenumber, the depth of the dimple holes was 39 μm. For the smaller diameter dimples used for the $m = 68$ "subcritical" azimuthal wavenumber, the depth of the dimple holes was proportionately small at 21 μm. We do not think the dimple depth is a critical parameter. For example, Reibert [1996] observed that for a fixed (subcritical) roughness spacing of z=12 mm, the total disturbance amplitude grew to a constant saturation amplitude even when the roughness height was varied from 6 to 48μ m. Although the initial disturbance amplitude increased with larger roughness, the effects downstream relaxed and yielded similar looking mode shapes. Additionally Reibert [1996] documented that as the roughness height increased from 6μ m to 18μ m, in 6μ m increments obtained by stacking the roughness elements, transition occurred at the same location for all three roughness heights.

3 Results

These results document the receptivity of the stationary cross-flow mode to the passive patterned roughness with critical and subcritical azimuthal wavenumbers. These controlled stability experiments are the first to be performed at a hypersonic Mach number with free-stream disturbance conditions in which the acoustic disturbances were not minimized through a "quiet" nozzle design. The experimental conditions are summarized in Table 1.

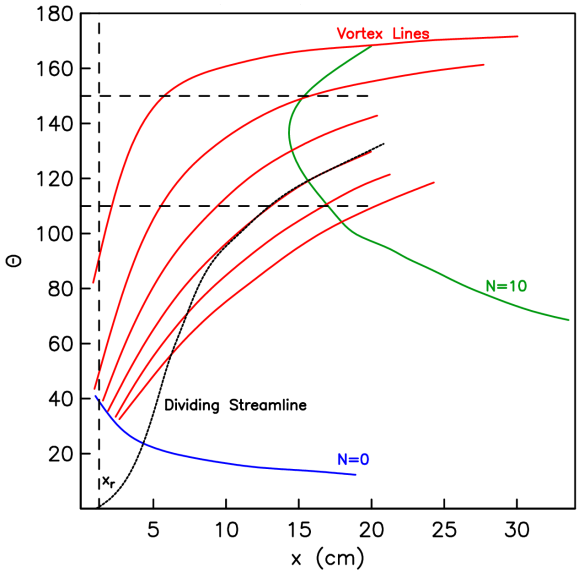

Figure 5: Linear stability and vortex path map used in determining axial location of discrete roughness for cross-flow transition control based on Li et al. [2010].

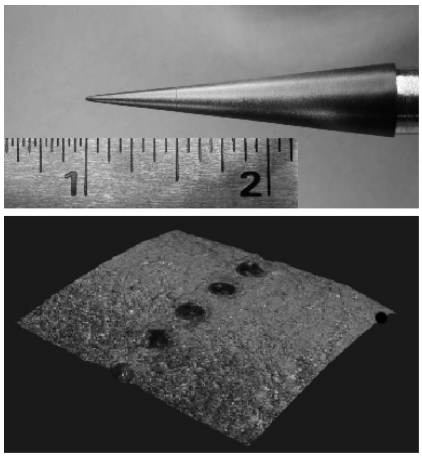

Figure 6: Photograph of a removable cone tip with representative "dimples" located at $x_r = 1.27$ cm. (0.5 in.) from the tip.

Table 1: Summary of Experimental Conditions

Mach No.	6.0
T_0 (K)	480
P_0 (bar)	11.5
Unit Reynolds Number (m^{-1})	10×10^6
Typical Run Time (ms)	80
Re_{x_r}	0.127×10^6
"Critical" Mode No.	45
"Subcritical" Mode No.	68

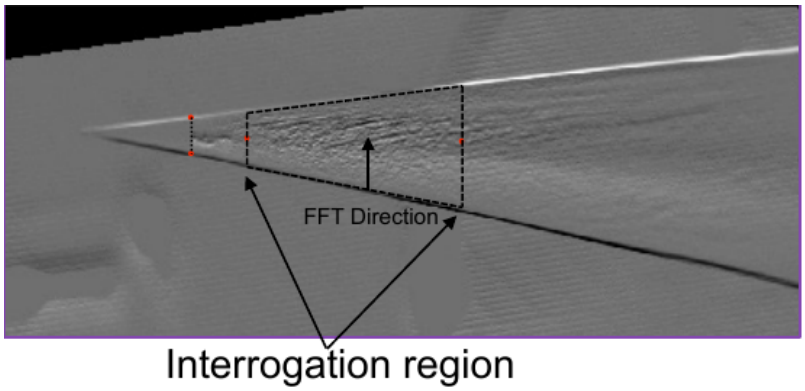

Figure 7: Sample processed image of oil flow surface visualization.

3.1 Surface Flow Visualization

The first objective was to verify that stationary cross-flow were observable under the conditions of the AFA facility. The key issue is that the AFA Ludwieg tube is a conventional design rather than a "quiet" design. There is no previous evidence in the literature of observations of stationary cross-flow modes in conventional (non-quiet) hypersonic wind tunnels. A possible reason is the potential dominance of traveling cross-flow modes, which are more amplified than the stationary modes, and sensitive to free-stream disturbances[Bippes, 1999].

Following Schuele et al. [2013], the presence of stationary cross-flow modes was first verified using surface oil-flow visualization. The approach was to apply to the surface of the cone a mixture of 15 parts 1000cSt Silicon oil, 5 parts Oleic acid and 1 part Titanium-Dioxide powder. The motion of the oil was recorded during the 80ms run time of the facility using a high-speed video camera. During the run, the oil pattern would reach a steady pattern that revealed the presence of the stationary cross-flow mode. Image processing was performed on selected frames of the videos. This included Sobol edge detection to highlight the stationary pattern, rotation of the image to account for the angle of attack, mapping of the curved surface onto a flat surface. Figure 7 shows a sample image following this processing. Spatial spectral analysis was then performed in the denoted interrogation region to determine the wavenumbers of features in the oil visualization image.

The azimuthal wavenumber distribution for the baseline (smooth tip) flow is shown in Figure 8. The dashed line at $m = 45$ represents the center of the band of most amplified stationary cross-flow modes based on Li et al. [2010]. The dot-dashed line indicates the axial location on the cone where transition would occur based on a linear theory N-factor of 10.

Figure 8 indicates a broad distribution of energy at wavenumbers that are approximately centered on $m = 45$, which is consistent with the linear theory predictions. The energy in this band of wavenumbers diminishes beyond the axial location of the N=10 line. This indicates that the coherent stationary pattern in the surface visualization is lost beyond this x-location, possibly as a result of turbulent transition. Using POD methods in the analysis of swept-wing boundary layer transition Glauser et al. [2014] indicated that the primary mode was still correlated downstream of the transition location. Therefore a more definitive estimate of the transition location will come from the off-wall total pressure measurements

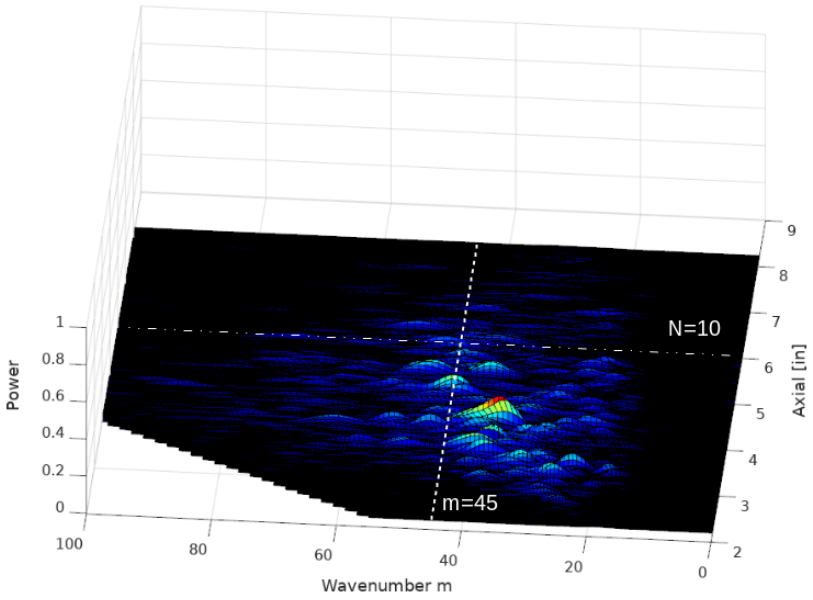

Figure 8: Azimuthal wavenumber spectrum axial distribution based on flow visualization for baseline cone (smooth tip) condition.

presented in the next section.

Similar surface flow visualization and image processing was performed for the cases with the "critical" and "subcritical" roughness cone tips. The wavenumber spectra for these are shown in Figures 9 and 10, respectively. Note that the amplitude scale on these spectra plots is the same as in Figure 8 for the smooth cone tip, to allow a direct comparison.

In contrast to the smooth tip case, the wavenumber spectra for the "critical" roughness cone tip shows a dominant peak at $m = 45$. This indicates that the stationary pattern in the surface visualization was well correlated with the $m = 45$ roughness wavenumber.

The wavenumber spectrum for the case with the "subcritical" ($m = 68$) roughness cone tip reveals a peak around $m = 68$ that was not previously evident with either the smooth cone tip, or the "critical" roughness tip. In addition, a broad peak near $m = 45$ is observed. The amplitude of this broad peak is approximately 30% lower than that with with the "critical" roughness tip, but larger than that with the smooth tip.

These wavenumber spectra of the surface flow visualization offers a first glimpse of the effect that the "subcritical" roughness might have on the transition location. If transition is defined as a loss of coherence of the stationary pattern, then for the "critical" roughness this appears to occur very close to the axial location where the N=10 line is drawn. In contrast with the "subcritical" roughness, well defined spectral peaks in wavenumber spectra exist well beyond the N=10 transition line. This might suggest that the transition has been suppressed by the "subcritical" roughness. Further evidence will come from off-wall Pitot probe measurements.

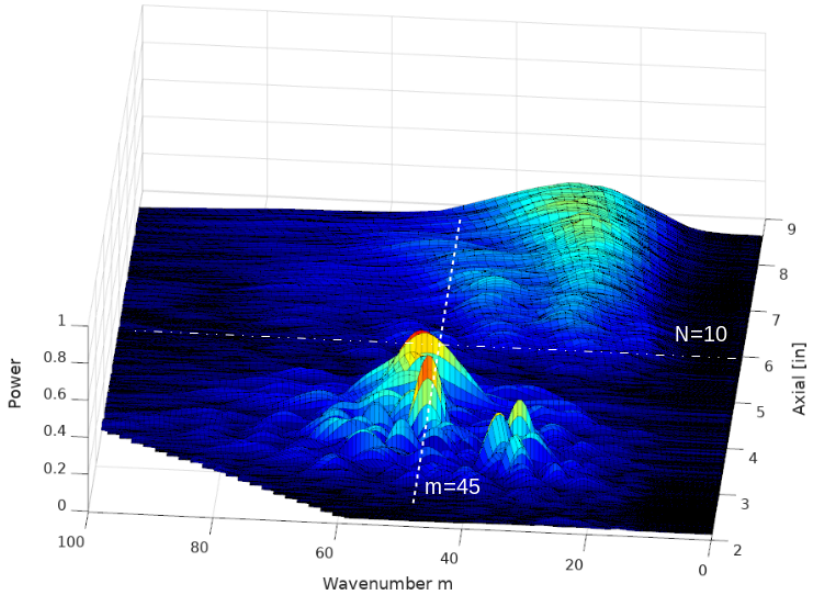

Figure 9: Azimuthal wavenumber spectra based on flow visualization for cone with "critical" ($m = 45$) roughness tip.

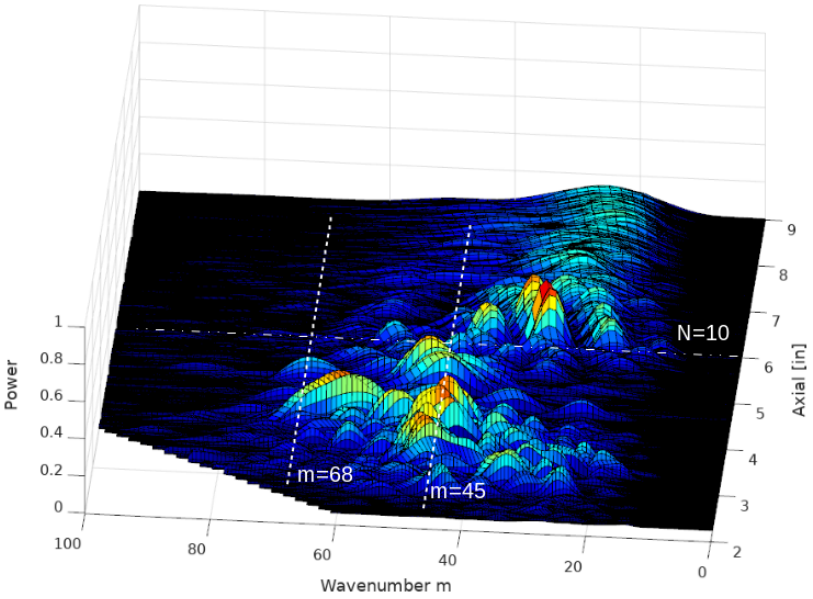

Figure 10: Azimuthal wavenumber spectra based on flow visualization for cone with "subcritical" ($m = 68$) roughness tip.

3.2 Pitot Probe Measurements

As described in Section 2, the Pitot probe response was frequency compensated out to 50 kHz, and sampled at 100 kHz. This was important not only to capture a sufficient number of time series points to obtain converged statistics within the short (80 ms) run times, but also to resolve the most amplified *traveling* cross-flow modes that were predicted[Li et al., 2010] to be centered at 35 kHz.

Total pressure time series were sampled at discrete (θ, x) locations at a fixed height above the surface of the cone. The data samples at each location represented one run of the facility. In total, there were on the order of 350 runs to generate the data presented in the following figures. For efficiency, the sampled locations were grouped in a range of spatial locations where transition was first expected to occur based on an N-factor of 10 that was indicated in Figure 5. This corresponded to $126^\circ \leq \theta \leq 143^\circ$, and $11.43\text{cm} \leq x \leq 17.78\text{cm}$.

To complement and validate the results from the surface flow visualization, the Pitot probe surveys were used to provide a direct measure of the mean flow distortion produced by the stationary cross-flow modes. This involved averaging the total pressure taken over the duration of a run at each (θ, x) location.

Figure 11(a) shows the azimuthal variation in the time-average total pressure at a fixed height above the cone surface with the "critical" ($m = 45$) roughness tip. A consequence of remaining at a fixed height, y, above the cone surface is that as the boundary layer thickens in the azimuthal direction along the lee side of the cone, the sensor moves deeper in the boundary layer so that y/δ is not constant. In order to better reveal the mean flow distortion produced by the stationary cross-flow modes, this mean trend has been removed. The color rendering of the total pressure is then presented as the deviation (plus or minus) about the local mean value. This clearly reveals the azimuthal variation in the total pressure that is indicative of the mean flow distortion produced by the stationary cross-flow mode. Note that negative mean-removed pressures correspond to a locally thickened portion of the boundary layer, and positive mean-removed pressures to locally thinned portions. The dotted curves in the figure traces out the x-development of two of the azimuthally thickened portions of the boundary layer. This trajectory should correspond to that of two neighbor stationary cross-flow vortices. As a check, these trajectories have been mapped to the curved coordinate and overlayed on the surface flow visualization image for the same "critical" roughness condition. The traces are drawn to the same scale as the image and shown in yellow. This shows a good correspondence between the azimuthal measurements of the total pressure and the flow visualization image.

The azimuthal wavenumber of the azimuthal pattern of positive and negative pressure shown in Figure 11(a) has an azimuthal wavelength of approximately 8° which coincides with that of the "critical" roughness, namely $360^\circ/45$. Evidence of this azimuthal wavenumber is further reinforced by the wavenumber spectra of this total pressure distribution that is shown in Figure 11(b). This shows a dominant peak at $m = 45$. The energy in the $m = 45$ mode decays to a minimum near the axial location where the N=10 factor predicts transition to occur. This agrees well with the wavenumber spectra that was derived from the flow visualization and shown in Figure 9.

The azimuthal variation in the total pressure indicative of the mean flow distortion pro-

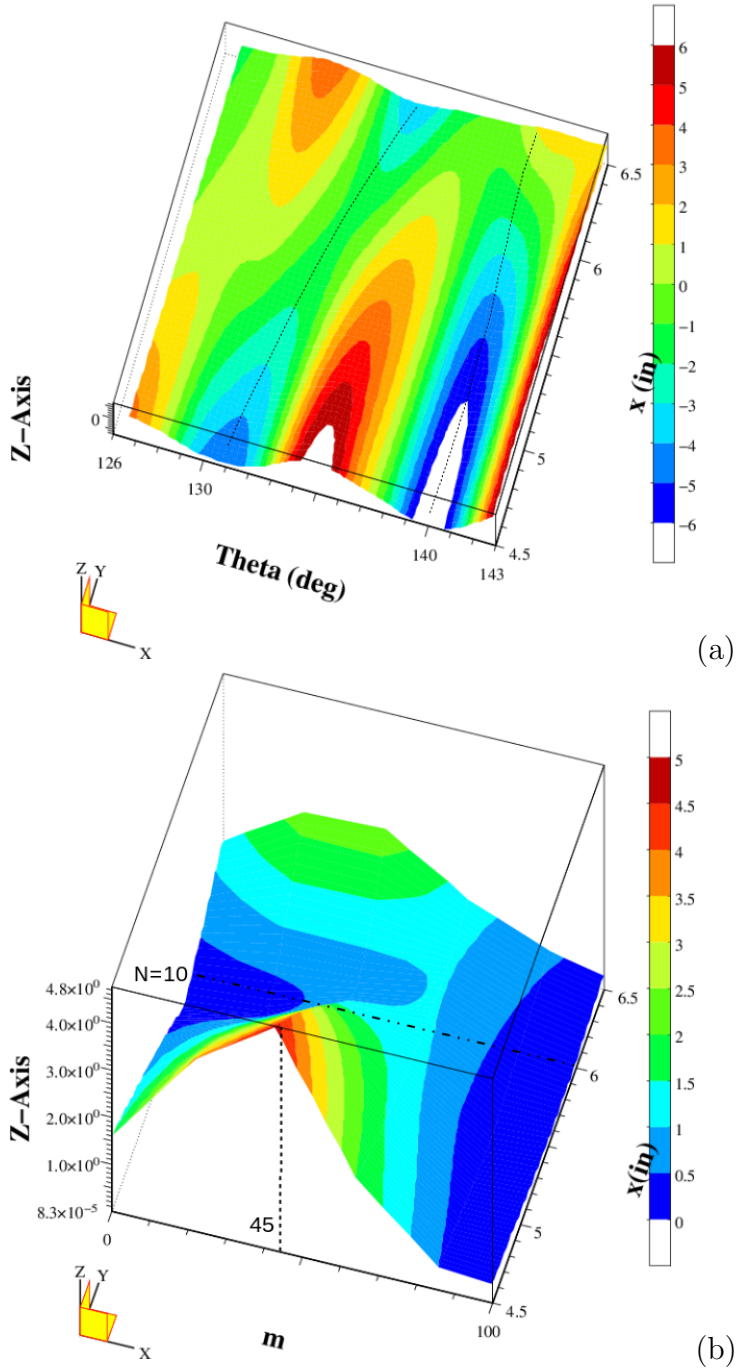

Figure 11: Azimuthal total pressure distributions at a constant height above the surface (a) and corresponding wavenumber spectra (b) for the case with the "critical" ($m = 45$) roughness cone tip.

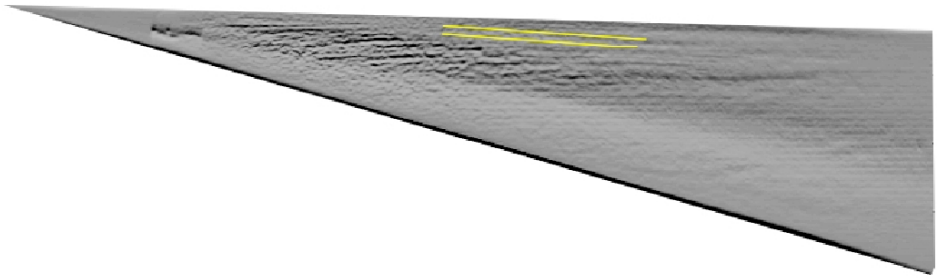

Figure 12: Overlay (yellow) of the (θ, x) trajectories of the mean flow distortion-thickened boundary layer in Figure 11(a) onto a surface visualization image for the same "critical" roughness condition.

duced by stationary cross-flow modes with the "subcritical" ($m = 68$) roughness is shown in Figure 13(a). The contrast with the "critical" roughness case is immediately apparent and reflects the higher azimuthal wavenumber (smaller azimuthal wavelength) that results from the closer spaced discrete roughness at the tip. For reference, the $m = 68$ mode has an azimuthal wavelength of 5.3°. The wavenumber spectra of the total pressure distribution for this roughness condition is shown in Figure 13(b). This shows a dominant peak at $m = 68$. Further downstream, the peak appears to shift to higher wavenumbers on the order of 100. This is consistent with Saric et al. [1998] where subcritical roughness with azimuthal wavenumbers of 1.5-times that of the critical roughness value would not generate subharmonic mode numbers. Similarly Schuele et al. [2013] observed only higher azimuthal wavenumbers generated by the "subcritical" roughness in their experiment at Mach 3.5.

The dominant peak in the wavenumber spectra with the subcritical roughness extends well downstream of the N=10 line, indicating that the transition Reynolds number has increased. As further evidence, the method of Schuele et al. [2013] was used to estimate transition location. This involved following the x-trajectory of a minimum in the total pressure distributions in Figures 11(a) and 13(a). The actual trajectories are shown by the dotted curves in those two figures. As previously mentioned, the pressure minima are indicative of a region of local thickening of the boundary layer. Such regions are known to develop an off-wall inflectional shear layer and subsequent inviscid instability that quickly leads to turbulence[Craig and Saric, 2016]. The starting azimuthal locations of both of these trajectories ($138° \leq \theta \leq 140°$)) is where the N-factor=10 curve is furthest upstream on the cone and therefore where transition is expected to occur first.

The x-development of the total pressure along the two pressure minima for the "critical" ($m = 45$) and "subcritical" ($m = 68$) roughness is shown in Figure 14. Estimates of the transition location were performed by two approaches. The first, shown in blue, followed a Preston tube approach in which a linear curve is fit to the rise in the total pressure near the wall that would accompany transition. The x-location where the linear curve intersects a common reference level is designated as the transition location. Based on this approach, the subcritical roughness resulted in a 25% increase in the transition location.

The second approach is based on the loss in the coherence of the mean flow distortion.

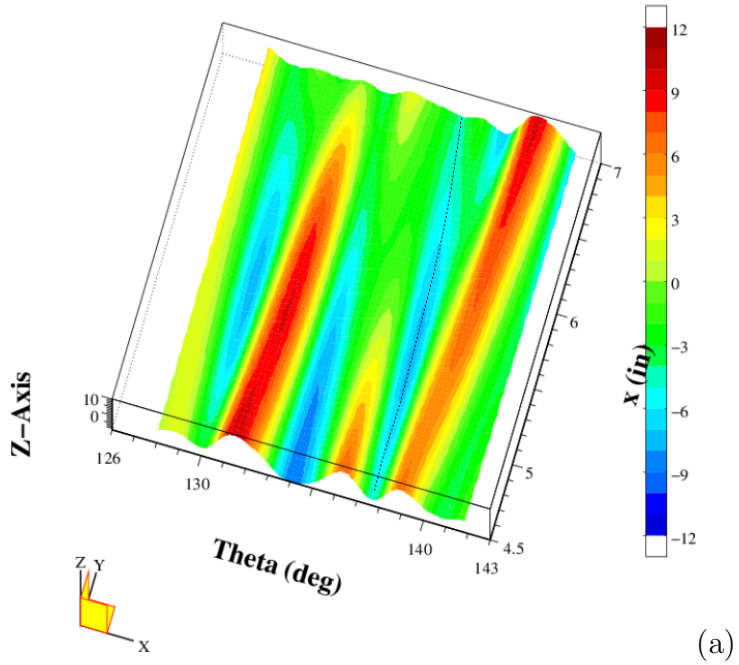

(a)

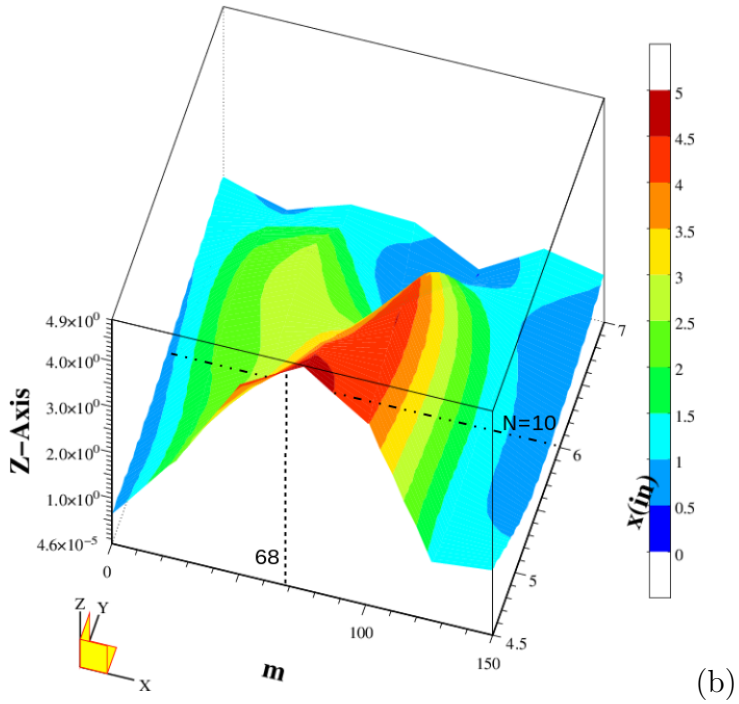

(b)

Figure 13: Azimuthal total pressure distributions at a constant height above the surface (a) and corresponding wavenumber spectra (b) for the case with the "subcritical" ($m = 68$) roughness cone tip.

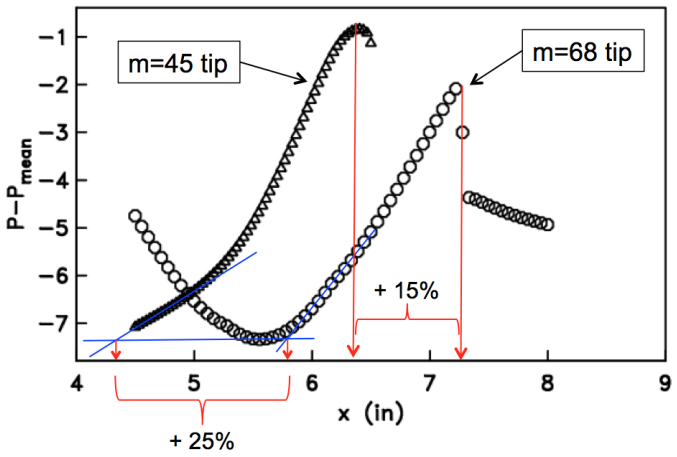

Figure 14: Axial distributions following pressure the minima denoted by the dotted curve in the total pressure distributions in Figures 11(a) and 13(a).

This would be evident as saturation and abrupt decay in the axial development of the total pressure. Based on this approach, shown in red, the subcritical roughness pattern resulted in a 15% increase in the transition location. Schuele et al. [2013] considered this as an indication of the *late stage* of transition, whereas the Preston tube approach was considered to be an indication of the *early stage* of transition.

As mentioned, the total pressure Pitot probes had a frequency response that was capable of detecting the traveling cross-flow modes. Figures 15 and 16 show spectra of off-wall total pressure fluctuations at increasing x locations for a single azimuthal angle for the critical and subcritical roughness cone tips. Both of these show a broad peak that is centered near 30 kHz that was predicted to be the frequency of the most amplified traveling cross-flow modes[Li et al., 2010]. The azimuthal wavenumber of the most amplified traveling mode is predicted[Li et al., 2010] to be $m = 40$.

The peak values of the spectra of the traveling disturbances, for all of the measured (θ, x) locations for the two tip roughness cases, were used to compile a view of the spatial amplitude distribution for the traveling cross-flow modes. These are shown for the critical $m = 45$ roughness cone tip in Figure 17, and for the subcritical $m = 68$ roughness cone tip in Figure 18. Examination of these reveals the presence of features with different azimuthal wavenumbers. To interpret these, one needs to consider possible interactions between the traveling and stationary cross-flow modes.

Physically, the traveling cross-flow modes ride (convect) over the stationary modes which then has the potential to modulate and interact with the traveling modes. Corke and Knasiak [1998b], Corke and Matlis [2006] and Corke et al. [2007] documented a nonlinear (quadratic) sum and difference interactions between traveling and stationary cross-flow modes in 3-D boundary layers over a rotating disk. The question is if there is similar interaction occurring in this instance.

Considering the "critical" roughness cone tip, the stationary modes were documented

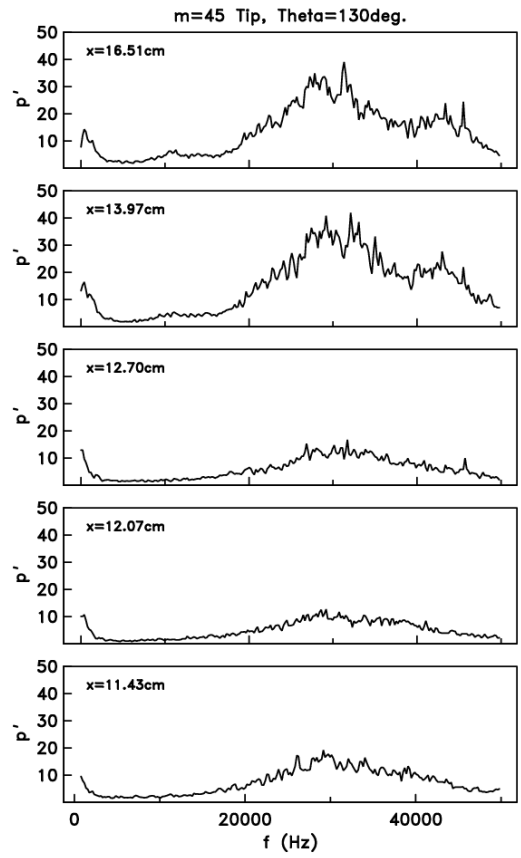

Figure 15: Spectra of traveling disturbances measured at different axial locations for a constant azimuthal angle for the "critical" ($m = 45$) roughness.

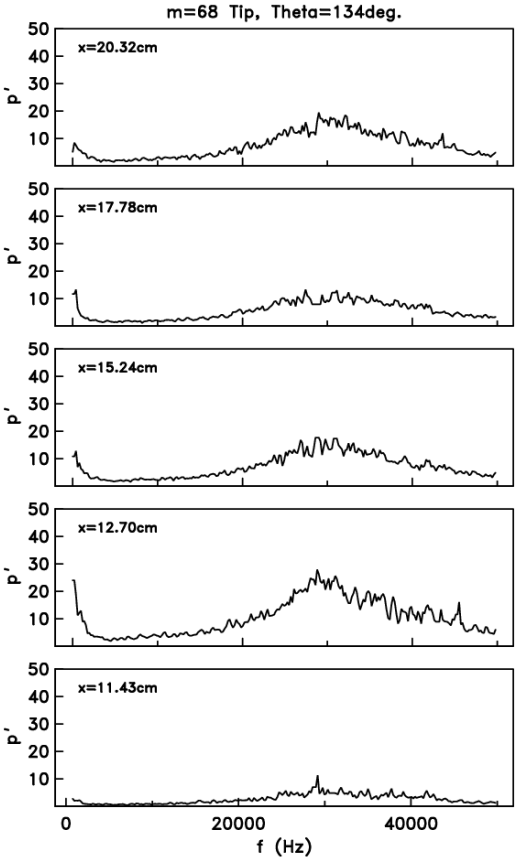

Figure 16: Spectra of traveling disturbances measured at different axial locations for a constant azimuthal angle for the "subcritical" ($m = 68$) roughness.

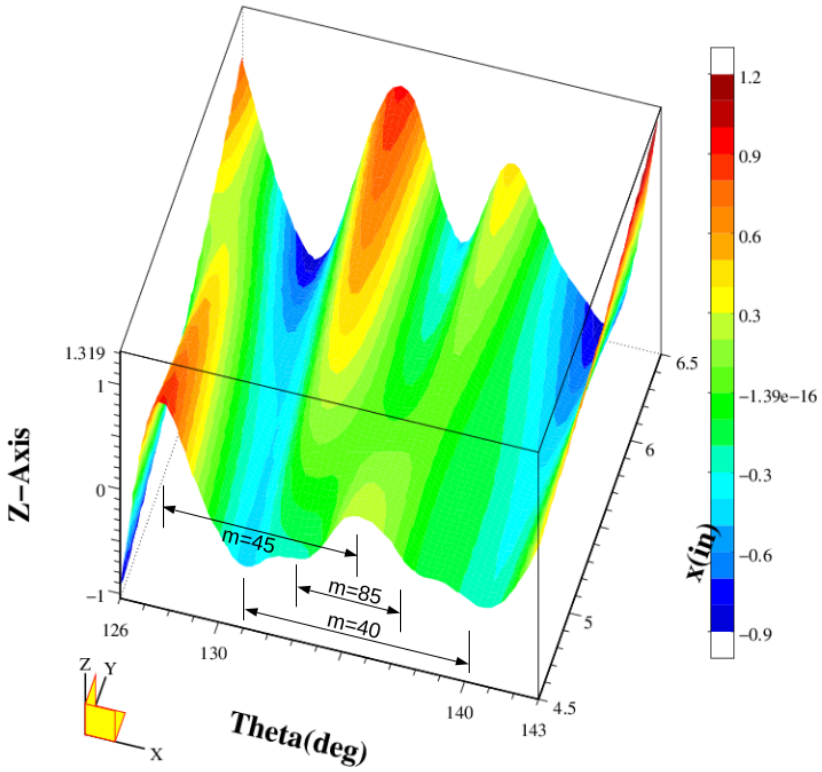

Figure 17: Spatial amplitude distribution of the spectral peak amplitude of the traveling disturbances for the "critical" ($m = 45$) roughness tip.

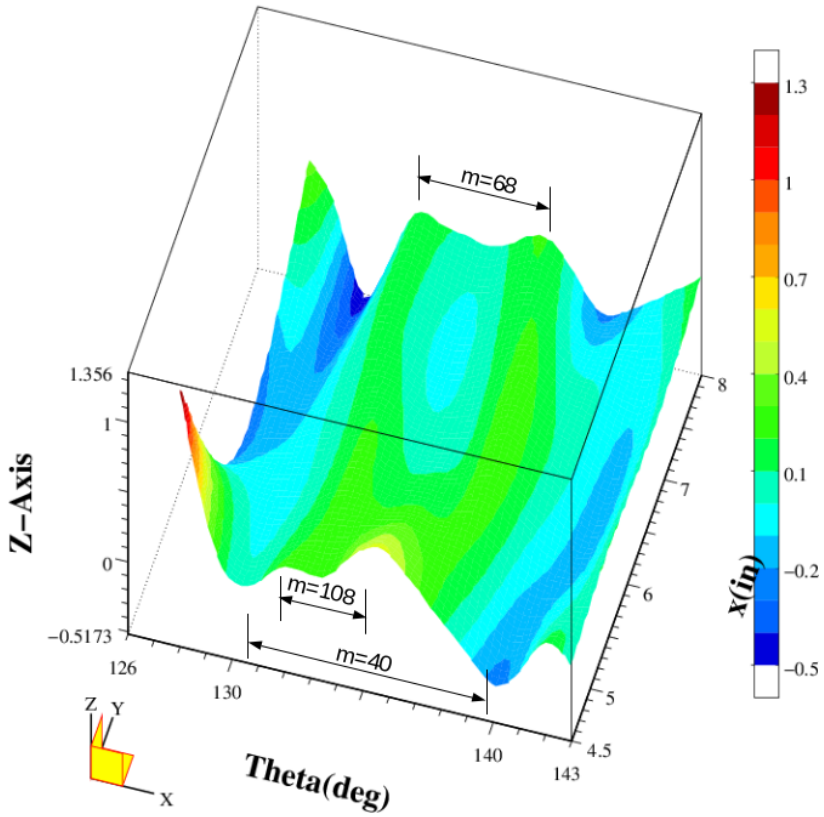

Figure 18: Spatial amplitude distribution of the spectral peak amplitude of the traveling disturbances for the "subcritical" ($m = 68$) roughness tip.

to occur at $m = 45$. This mode will be designated as $(0, 45)$, where the first index is the frequency, and the second is the azimuthal wavenumber.Li et al. [2010] determined the most amplified traveling cross-flow mode occurred with an azimuthal wavenumber of $m = 40$. This mode will be designated as $(f_t, 40)$, where f_t refers to the frequency of the traveling mode which Figures 15 and 16 found to be centered about 30 kHz.

The first interaction between these two modes will be through a sum and difference, namely

$$(0, 45) \pm (f_t, 40) = (f_t, 85) \text{ and } (f_t, 5). \tag{1}$$

Both $(f_t, 85)$ and $(f_t, 5)$ are traveling modes with the same frequency as the primary traveling mode. Therefore the amplitude of the spectral peak in Figure 17 should be representative of not only the primary traveling mode, but also the sum and difference modes that occur at the same frequency.

Now the result of the summing interaction, $(f_t, 85)$, would have an azimuthal wave angle of approximately 4°. That of the difference interaction, $(f_t, 5)$, would have an azimuthal wave angle of 72°. The latter is larger than the azimuthal extent of the measurements. However the former, $(f_t, 85)$, is distinguishable in the spatial amplitude distribution in Figure 17.

Also observable is a spatial amplitude distribution with an azimuthal wavenumber that matches that of the discrete roughness, $m = 45$. This is not realizable through a quadratic interaction to produce $(f_t, 45)$. Therefore it is most likely due to a *linear* superposition that leads to a modulation of the traveling mode amplitude as it rides over the stationary mean flow distortion. Such behavior has in fact been identified through Direct Navier Stokes simulations of subsonic 3-D boundary layers undergoing cross-flow instability by Dörr et al. [2017].

For the case with the "subcritical", $m = 68$ roughness cone tip, the sum and difference interaction would be

$$(0, 68) \pm (f_t, 40) = (f_t, 108) \text{ and } (f_t, 28). \tag{2}$$

Here $(f_t, 108)$ would have an azimuthal wave angle of approximately 3°, and $(f_t, 28)$ an azimuthal wave angle of approximately 13°. Both again are traveling modes with the same frequency as the primary traveling mode. Both of these are evident in the spatial amplitude distribution shown in Figure 18.

As before, a spatial amplitude distribution with an azimuthal wavenumber that matches that of the discrete roughness, $m = 68$, is also observable. This again is most likely due to a linear superposition that produces a modulation of the traveling mode amplitude as it rides over the stationary mean flow distortion produced by the $m = 68$ roughness.

An attempt has been made to quantify these sum and difference interactions by determining the degree of phase locking between the primary stationary and traveling cross-flow modes and their sum and difference modes. This utilized the cross-bicoherence statistic previously used in documenting nonlinear interaction between stationary and traveling cross-flow modes in the boundary layer over a rotating disk[Corke and Matlis, 2006, Corke et al., 2007]. The cross-bicoherence (CBC) is defined as

$$\beta_{ijk}(m_1, m_2) = \frac{|\tilde{R}_{ijk}(m_1, m_2)|^2}{< |\tilde{p}_i(m_1)|^2 |\tilde{p}_j(m_2)|^2 >< |\tilde{p}_k(m_3)|^2 >} \tag{3}$$

where

$$\tilde{R}_{ijk}(m_1, m_2) =< \tilde{p}_i(m_1)\tilde{p}_j(m_2)\tilde{p}_k^*(m_3) > \tag{4}$$

is the cross-bispectrum, with i, j and k equal to either i or j that refer to one of the two mean-removed pressure time series, p, with azimuthal wavenumbers m_1, m_2 and m_3, respectively. The notation $(||)$ is the modulus of the component, $\sim$ denotes the Fourier transformed function in wavenumber domain, $<>$ represents the ensemble average. These wavenumbers are related to each other such that $m_1 + m_2 + m_3 = 0$.

In the experiment, one of the data series used in the CBC was the azimuthal variation in the time-averaged total pressure, $\bar{p}(\theta)$, at a selected x location on the cone. The same data were used to generate Figures 11(a) and 13(a). This data series therefore represents the azimuthal mean flow distortion at one x location. The Fourier transform of this data series is $\tilde{\bar{p}}(m)$. The wavenumber spectra shown in Figures 11(b) and 13(b) correspond to $|\tilde{\bar{p}}(m)|^2$ at each x location.

The second data series used in the CBC corresponds to the total pressure time series before time averaging, $p(t)(\theta)$, at the same x location as $\bar{p}(\theta)$. This data series contains pressure fluctuations that correspond to the traveling cross-flow modes. The squared modulus of the transformed data series, $|\tilde{p}(f)|^2$, was used to generate the frequency spectra that were shown in Figures 15 and 16.

It is necessary that the two transformed data series have the same independent variable units. In $|\tilde{p}(m)|^2$, the independent variable is azimuthal wavenumber, m. In $|\tilde{p}(f)|^2$ the independent variable is frequency, f. Therefore in the case of the latter, we chose to convert frequency to azimuthal wavenumber. As previously pointed out, analysis from Li et al[Li et al., 2010] indicated that the azimuthal wavenumber in the center of the most amplified band of frequencies of traveling cross-flow mode (35 kHz) was $m = 40$. This was used as a point of reference to the conversion from frequency to wavenumber of the traveling mode data series.

Another important step in computing the CBC was that the sampling rates be the same for the two data series. For the time series representing the stationary cross-flow mode, $\bar{p}(\theta)$ (data series 1), the sampling rate was 8.54 pts/$\circ$. For the time series representing the traveling cross-flow mode (data series 2), the sampling rate was considerably less at 0.317 pts/$\circ$. Therefore in order to match the two data sampling rates, data series 2 was zero-padded by the appropriate amount prior to the Fourier transform.

As with linear coherence, the value of the CBC varies between 0 and 1. High values of the CBC indicate a high degree of triple phase locking

$$\theta_i(m_1) + \theta_j(m_2) = \theta_k(m_3) \tag{5}$$

from realization to realization. Here $\theta_i(m_1)$ is the instantaneous circular phase angle of $\tilde{p}_i(m_1)$.

The region of validity of the CBC is set by the Nyquist criterion, where the sum of any two frequencies (or wavenumbers in this case) cannot exceed half the sampling rate. This region then takes the form of two isosceles triangles, one each for sum and difference interactions. The outline of the two triangles defining the valid regions is shown in Figures 19 and 20. The region of interest has been enlarged to focus on the two summing interactions

between the stationary and traveling cross-flow modes that was postulated for the "critical" and "subcritical" roughness tips.

For the CBC shown in Figures 19 and 20, the data series (1) corresponding to the stationary cross-flow modes is designated by subscript 1, with its wavenumber read from the abscissa. The data series corresponding to the traveling cross-flow modes is designated by subscript 2, with its wavenumber read from the ordinate. The ordinate wavenumbers are either added (top triangle) or subtracted (bottom triangle) from those read on the abscissa to give the third frequency which is read as the intercept of a $-45°$ line to the abscissa. This method for reading the CBC is outlined by the yellow arrows for the summing interaction in the two figures.

The decision of which of the two data series (1 or 2) corresponds to the i, j and k series in the calculation of $\beta_{ijk}(m_1, m_2)$ in Equation 3 is important. For example if $[i, j, k]$=[1,1,1] the CBC would indicate wavenumbers in data series 1 that result from sum and difference interactions in data series 1. This is referred to as the auto-bicoherence. Similarly this could only involve data series 2 where $[i, j, k]$=[2,2,2]. Based on the results in Figures 17 and 18, that indicate an influence of the stationary cross-flow mode on the spatial amplitude distribution of the traveling cross-flow mode, we chose the order $[i, j, k]$=[1,2,2]. Thus we were investigating an interaction between the stationary mode (1) and the traveling mode (2) that results in sum and difference traveling modes (2).

The CBC statistic involved 256 ensembles. Figure 19 corresponds to the "critical" roughness case. The (x, θ) location corresponds to the most upstream measured location ($x = 11.43$ cm), and an azimuthal location ($\theta = 135°$) where the spatial amplitude at the center frequency of the traveling cross-flow mode (35 kHz) was at a peak level as shown in Figure 17. The CBC at that location indicates a significant triple phase locking between the stationary cross-flow mode generated by the "critical" ($m = 45$) roughness, and the traveling cross-flow mode with azimuthal wavenumber ($m = 40$) to produce a traveling cross-flow mode with an azimuthal wavenumber of $m = 85$. This is a strong indication that the $m = 85$ variation in the spatial amplitude distribution in Figure 17 is the result of a nonlinear interaction between the stationary and traveling cross-flow modes.

The CBC does not reveal the difference interaction between the stationary and traveling modes that would result in the traveling mode at $m = 5$. The azimuthal span of the measurements in Figure 17 was insufficient to indicate if there was an azimuthal amplitude variation of this traveling mode with this mode number. Therefore based on the CBC alone, there is no evidence of this difference interaction.

Finally the CBC reveals strong triple phase locking in summing interactions between higher stationary wavenumbers and a broad range of wavenumbers of traveling modes. The higher stationary wavenumbers might represent uncontrolled surface roughness on the cone tip. If this is the case, it points to a mechanism for spectral broadening. However, a large CBC only indicates phase locking. It does not indicate the level of energy in these modes. Based on the spectra that were shown in Figure 15, the dominant traveling mode is centered near 30 kHz and associated with $m = 40$.

The CBC for the "subcritical" roughness case is shown in Figure 20. The (x, θ) location again corresponds to the most upstream measured location ($x = 11.43$ cm). The azimuthal

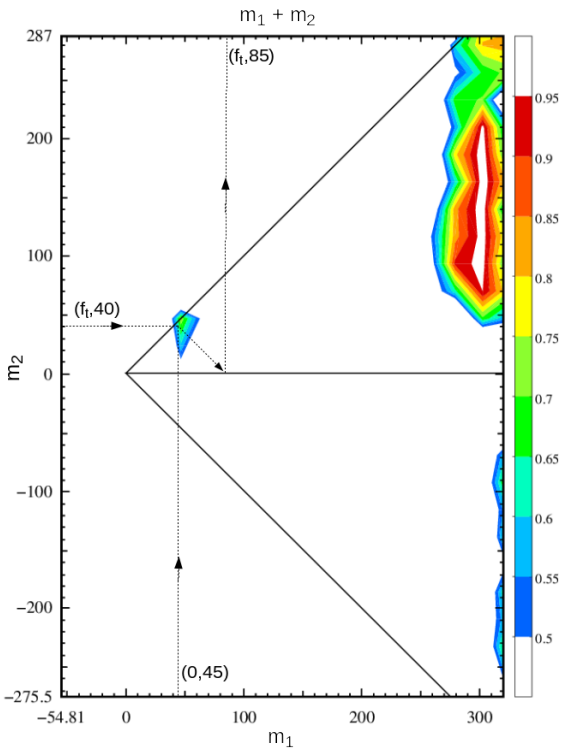

Figure 19: CBC for "critical" roughness case indicating triple phase locking for $(0, 45) + (f_t, 40) = (f_t, 85)$. Measured at $(x, \theta) = (4.5\text{in.}, 135°)$

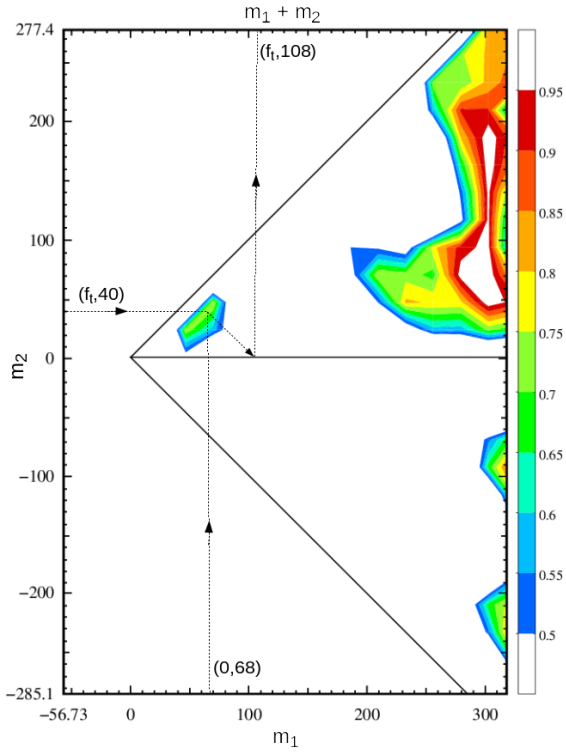

Figure 20: CBC for "subcritical" roughness case indicating triple phase locking for $(0, 68) \pm (f_t, 40) = (f_t, 108)$. Measured at $(x, \theta) = (4.5\text{in.}, 138°)$

location was $\theta = 138°$, which was close to the spatial amplitude peak at that x-location in Figure 18, and aligned with the peak having the discrete roughness $m = 68$ spacing at the downstream location. In this case, the CBC indicates a significant triple phase locking between the stationary cross-flow mode generated by the "subcritical" ($m = 68$) roughness, and the traveling cross-flow mode with azimuthal wavenumber ($m = 40$) to produce a traveling cross-flow mode with an azimuthal wavenumber of $m = 108$. Therefore there is a strong indication of a nonlinear interaction between the stationary and traveling cross-flow modes that in this case results in a traveling mode with an azimuthal wavenumber of $m = 108$.

The azimuthal amplitude distribution for the traveling cross-flow mode in Figure 18 had also revealed a variation with azimuthal wavenumber of $m = 28$ that could have been the result of a nonlinear difference interaction between the stationary and traveling cross-flow modes. As with the previous case, the CBC in Figure 20 does not reveal a difference interaction leading to $m = 28$. As with the previous case, the CBC indicates strong triple phase locking between higher stationary mode azimuthal wavenumbers and a broad band of traveling mode wavenumbers. As before, based on the traveling mode spectra in Figure 16, the lower energy in these higher mode numbers makes it more likely that the phase-locked interactions near the most amplified traveling mode wavenumber will dominate at transition.

4 Discussion: Transition Control

The surface flow visualization and off-wall azimuthal surveys of the total pressure revealed the same picture of the mean flow distortion produced by the stationary cross-flow modes that developed in the boundary layer over the right-circular cone at the 6° angle of attack. These measurements confirmed the receptivity of the cross-flow mode to the discrete roughness in a conventional (non-quiet design) environment.

The design of the roughness was identical in all characteristics to that used by Schuele et al. [2013] in a quiet Mach 3.5 tunnel. The passive roughness consisted of micron-size indentations (dimples) that were located near the cone tip, just upstream of the first neutral growth branch of stationary cross-flow modes, based on linear stability analysis. The roughness dimples encircled the cone tip with a uniform spacing that defined the azimuthal wavenumber of the roughness. The disturbances produced by the roughness dimples were expected to follow the theoretical vortex path lines to the azimuthal region where turbulent transition was predicted to first occur based on linear theory N-factors. For the cone at a 6° angle of attack, this was expected to be in the range of azimuthal angles from 110° to 150°, measured from the windward stagnation line. As a result, although the dimples encircled the cone tip, only those that intersected with the theoretical vortex path lines at the axial location of the roughness were active.

Two azimuthal wavenumbers of roughness were investigated. One was in the band of the initially most-amplified ("critical") wavenumbers of stationary cross-flow modes. The other was at a 1.5 times higher ("subcritical") wavenumber. The "critical" wavenumber roughness was intended to represent a controlled baseline that would favor a single wavenumber stationary cross-flow mode. The "subcritical" wavenumber roughness was intended to suppress the growth of initially amplified stationary cross-flow modes and thereby increase the tran-

sition Reynolds number in a scenario first documented at subsonic Mach numbers by Saric et al. [1998].

A smooth cone tip representing an uncontrolled baseline was documented only through surface flow visualization. This was the only viable approach for a full-field survey without a defined roughness pattern that was fixed from one run to the next in the Ludwieg tube. This however did reveal a stationary pattern with azimuthal wavenumbers that were in the band predicted to be most amplified from linear theory by which our "critical" roughness was selected. The transition location with the smooth tip was also in good agreement with that for the critical roughness, suggesting that the disturbance amplitude of the critical roughness was comparable to that of random roughness on the smooth tip.

Transition for the smooth cone tip, and that with the "critical" roughness, indicated an N-factor of 10 near transition. This was similar to that observed by Schuele et al. [2013] in a "quiet" Mach 3.5 flow. One might expect that in the present results in the conventional non-quiet AFA tunnel, transition might occur earlier compared to the quiet tunnel. The free-stream disturbances could be any combination of entropy, vorticity, and acoustic fluctuations, however in hypersonic tunnels, vorticity is highly stretched and damped leaving primarily entropy and acoustic fluctuations. With regard to stationary cross-flow modes, evidence at subsonic Mach numbers indicates a lack of sensitivity to acoustic disturbances[Radeztsky Jr. et al., 1999]. Therefore we might not expect any difference between the cross-flow transition N factors for "quiet" and "noisy" tunnels. The results appear to supported that conclusion.

A corollary to that discussion is that in the process of transition of the stationary cross-flow modes, the resulting mean flow distortion develops high shear layers[Craig and Saric, 2016] that are then inviscidly unstable, and susceptible to acoustic disturbances. Therefore this might provide a mechanism by which transition might be hastened in a conventional, non-quiet, tunnel. However being an inviscid instability, the high amplification rate would lead to a rapid transition in a short distance that could be imperceptible in comparison to that in a "quiet" tunnel.

Transition front measurements using the Preston tube approach indicated that the transition Reynolds number had increased by approximately 25% with the "subcritical" wavenumber roughness compared to the "critical" wavenumber roughness. This is less than the 40% increase in the transition Reynolds number in the Mach 3.5, quiet environment documented by Schuele et al. [2013]. Given that the roughness design was the same in both experiments, one can question if

1. the difference in the increase in transition Reynolds number was due to a Mach number effect, or

2. if the difference is due to the difference in acoustic disturbance levels between the experiments.

With regard to the latter, Neel et al. [2018] have investigated the effect of free-stream disturbances on stationary cross-flow modes on elliptic cones. The disturbance levels were varied based on the position of the model within the nozzle expansion. The presence of stationary cross-flow modes was determined by thermal imaging where they appeared as elevated temperature streaks. They observed that the lower disturbance level produced more

distinct streaks compared to the higher disturbance condition. Neel et al. [2018] observed that the streak formation at their lower disturbance condition compared well with that obtained on the same geometric model under "quiet" conditions[Juliano and Schneider, 2010].

Neel et al. [2018] had also investigated transition on their elliptic cone model in a "quiet" tunnel. The thermal images revealed extremely sharp hot streaks that suggested well defined stationary cross-flow vortices. Model surface pressure measurements in the quiet tunnel environment showed energy in a band of frequencies centered about 40 kHz. that is expected to be due to traveling cross-flow modes.

The locations of the streaks in the thermal images, associated with the stationary cross-flow modes in the Neel et al. [2018] experiments did not always coincide with the azimuthal locations of the surface pressure sensors. This then offered a means of assessing any azimuthal variation in the amplitude of the 40 kHz traveling cross-flow mode in their experiments. In particular, their Run 3180 reveals such an azimuthal variation that could be evidence of an interaction between the traveling and stationary cross-flow modes.

The origin of the stationary cross-flow modes in experiments like that of Neel et al. [2018], and Juliano and Schneider [2010] are expected to be due to randomly distributed surface roughness. In contrast, the patterned discrete roughness used in the experiments by Schuele et al. [2013] and the present experiments was fixed. This controlled roughness initial condition offered a more quantitative approach to explore possible interactions between the traveling and stationary cross-flow modes. Such an approach followed that used by Corke and Matlis [2006] and Corke et al. [2007] in the canonical cross-flow transition that occurs on a rotating disk.

The evidence of an interaction between the stationary and traveling cross-flow modes is embodied in the spatial amplitude distributions for the two roughness cases that was shown in Figures 17 and 18. Recalling that these were the result of hundreds of individual wind tunnel runs, with the only constant, besides Reynolds number, being the controlled discrete roughness on the model, the coherent pattern in the spatial fluctuation amplitude is remarkable.

The spatial amplitude distribution showed evidence of a quadratic interaction between the linearly amplified traveling and stationary cross-flow modes. For the critical roughness with frequency and mode number of $(0, 45)$, this led to the generation of a traveling mode $(f_t, 85)$ with the same frequency as the primary traveling mode, f_t. The quadratic interaction between $(f_t, 85)$ and the stationary and the primary traveling modes was confirmed with the CBC statistic. The $(f_t, 85)$ mode resulted from a summing interaction. One would expect a similar difference interaction that would lead to a traveling mode $(f_t, 5)$. However, this was not confirmed in the experiment. If the difference mode, $(f_t, 5)$, were to occur, then an interaction with the summed mode, $(f_t, 85)$, could produce a harmonic traveling mode, $(2f_t, 90)$, and a higher wavenumber stationary mode, $(0, 80)$. Evidence of the latter might be found in the thermal images of Neel et al. [2018] or Juliano and Schneider [2010].

This process of successive interactions can be a mechanism to spread energy that leads to a broad spectrum associated with turbulence. Such a broadening spectrum was apparent in the wavenumber spectra based on the surface flow visualization and off-wall pressure measurements that were shown in Figures 9 and 10, and Figures 11(b) and 13(b) for the

discrete roughness cases.

The strength of these interactions will depend on the initial amplitude of the *traveling* cross-flow modes. Evidence indicates that this depends on the free-stream disturbance level that particularly includes vortical disturbances, and possibly acoustic disturbances. If one excludes Mach number effects, the difference between the degree of transition suppression between the experiments of Schuele et al. [2013] and the present experiments is likely only the level of acoustic disturbances. The potentially larger amplitude traveling cross-flow modes in the higher acoustic environment, and the nonlinear interaction with the stationary mode, could hasten transition, and reduce the effectiveness of the subcritical roughness. In a broader sense, this interaction between stationary and traveling cross-flow modes might account for the difference between the transition Reynolds number in conventional (noisy) and quiet hypersonic wind tunnels.

5 Effect of Controlled Traveling Mode Forcing

The observation of the quadratic interaction between the stationary and most amplified traveling cross-flow modes, and the speculation that the lower degree of transition suppression was the result of higher acoustic disturbance levels in the conventional (non-quiet) tunnel prompted a follow-on experiment in which the amplitiude of the traveling modes might be directly varied. The general objectives were then to

1. seek to control the initial amplitude of the traveling cross-flow modes, while at the same time introducing controlled stationary cross-flow modes,

2. documenting the effect this had on the nonlinear interaction between stationary and traveling cross-flow modes and spectral broadening, and

3. document the overall effect that the traveling mode initial amplitude had on the transition Reynolds number.

The approach to introduce controlled unsteady disturbances in the boundary layer was based on the previous design by Schuele et al. [2013]. In their case, a plasma actuator was designed to produce stationary cross-flow modes similar to the passive roughness. The approach was successful, demonstrating amplitude control of the stationary cross-flow modes for both "critical" and "subcritical" wavenumbers. In the present case, we sought to introduce *controlled unsteady disturbances* at a frequency that would be in the most amplified band of traveling cross-flow modes. The stationary cross-flow modes would be excited in the same manner as before, utilizing an azimuthal array of dimples located just upstream of the lower instability branch. However in the present case, only the "critical" ($m = 45$) azimuthal wavenumber roughness was investigated. Figure 21 shows photographs of the unassembled and assembled components of the cone tip that combines a roughness dimple array to excite stationary cross-flow modes at the critical wavenumber ($m = 45$), and a plasma actuator ring to introduce an unsteady disturbance at a specific frequency.

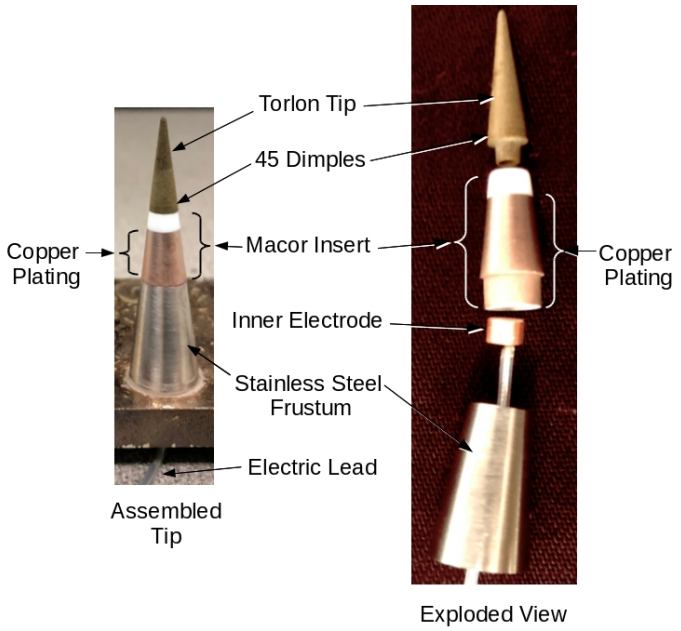

Figure 21: Photographs of exploded assembly view and fully assembled view of cone tip that combines dimples for stationary mode forcing and a plasma ring for traveling mode forcing.

The plasma actuator requires two electrodes separated by a dielectric material. The dielectric material in this case is Macor, a machineable ceramic. The Macor forms the middle section of the conical tip. The internal electrode consists of a cylindrical brass segment that is located inside a bored out hole in the center of the Macor section. A wire lead that passes through the center of the cone tip provides the AC electric connection to the internal electrode. The external electrode was formed by plating copper onto the surface of the Macor portion of the cone tip. The copper plating was vapor deposited to a thickness of $90nm$. The r.m.s. surface roughness variation of the copper plating was verified to be well below that of the roughness dimples.

The copper plating wrapped completely around the Macor portion of the tip. It extended from approximately 0.2 mm downstream of the roughness dimples to the base of the Macor portion of the cone tip, where on assembly, it contacted a stainless-steel base. This contact to the stainless-steel provided an electrical connection to the metal cone model, which was earth grounded. This provided a current path to ground for the plasma actuator.

The hardness of the Macor made it impossible to apply the roughness "dimples" onto its surface. Therefore the leading portion of the cone tip was made from Torlon 5530, which is the same material previously used for the roughness tips. The Torlon tip mounted to the leading part of the Macor portion of the tip. The fully assembled tip is shown in the left part of Figure 21.

Figure 22 shows the roughness/plasma actuator cone tip operating in the Air Force Academy Mach 6 Ludwig tube during a run. The plasma actuator frequency was 35 kHz, which is in the center of the most amplified band based on linear theory, and verified in the

previous experimental results that were shown in Figures 15 and 16. The plasma (ionized air) appears as a purple ring around the cone tip. The left photo shows the plasma under ambient light. The right photo shows the plasma in the darkened lab.

The plasma actuator was started before initiating the tunnel run. In the Air Force Ludwieg tube operation, this was with the test section at the vacuum pressure. The plasma actuator was left on through the run, and then turned off after the completion of the run. The AC peak-to-peak voltage was kept constant at 5kV.

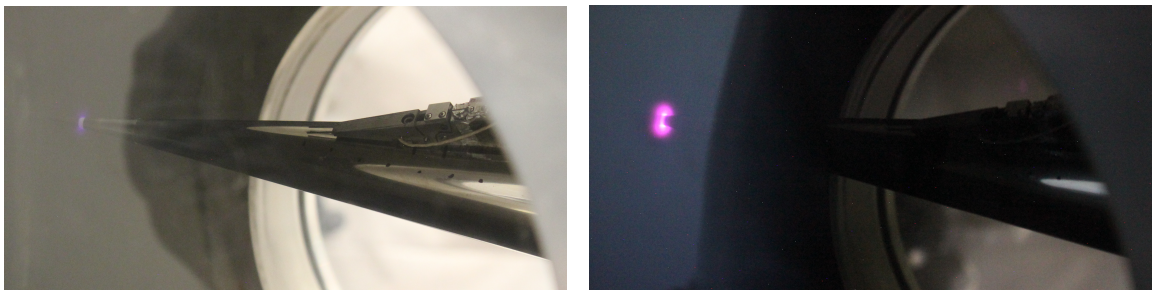

Figure 22: Photographs of cone tip with plasma actuator operating in the Mach 6 flow. Top view is with ambient light and bottom view is with the lab darkened.

The experiments were conducted with the same conditions as the previous tunnel entries. These are listed in Table 1. The measurements consisted of total-pressure time series taken at a fixed height above the surface of the cone. The azimuthal extent was $130^\circ \leq \theta \leq 140^\circ$ in increments of 1°, and an axial extent of $10.16\text{cm} \leq x \leq 16.51\text{cm}$ (4.0 to 6.5 inches) in increments of 1.27 cm (0.5 in.). The azimuthal extent was slightly smaller than in the previous experiments in order to reduce the number of tunnel runs and subsequently tunnel time. However the axial extent was increased slightly to account for the faster development of the mean flow distortion with the plasma actuator excitation.

Evidence that the boundary layer was receptive to the plasma actuator 35 kHz excitation is shown in Figure 23. This shows a comparison of the frequency spectra of the total pressure fluctuations with the plasma actuator excitation off and on. The ordinate of the spectra plot is normalized rms pressure fluctuations. The dashed curve corresponds to the baseline condition with the plasma actuator off. This shows the previously determined band of frequencies associated with the traveling cross-flow modes. The solid curve shows the spectrum with the plasma actuator operating at 35 kHz. This shows a distinct peak at 35 kHz (marked by the vertical dashed line), as well as an increase in the pressure fluctuations across the band associated with the traveling cross-flow modes. These spectra correspond to $x = 5.5$ in. and $\theta = 140^\circ$. As will be apparent in subsequent results, the appearance of the spectral peak and side-band fluctuations has a spatial distribution that is consistent with an interaction between the traveling and stationary cross-flow modes.

The Pitot probe surveys were again used to provide a direct measure of the mean flow distortion produced by the stationary cross-flow modes. This involved averaging the total pressure time series taken over the duration of a run at each (θ, x) location.

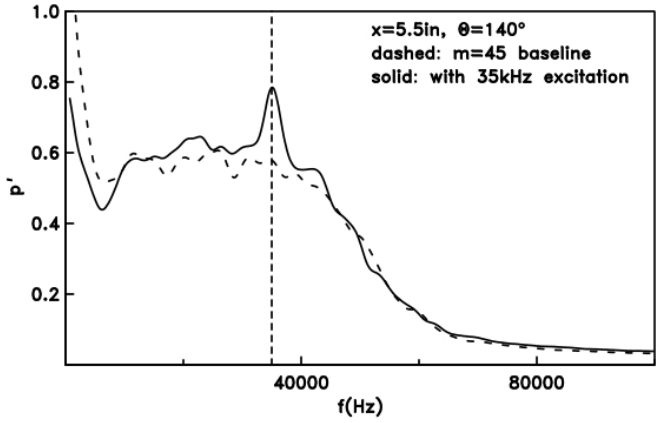

Figure 23: Sample comparison of spectra of pressure fluctuations at x=5.5in. and $\theta = 140°$ without and with plasma excitation at 35 kHz.

Figure 24(a) shows the azimuthal variation in the time-average total pressure at a fixed height above the cone surface with the "critical", $m = 45$, roughness tip. As before, the effect of the azimuthal variation in the average total pressure due to the azimuthally thickening boundary layer has been removed. The color rendering of the total pressure is then presented as the deviation (plus or minus) about the local mean value. This clearly reveals the azimuthal variation in the total pressure that is indicative of the mean flow distortion produced by the stationary cross-flow mode. As a reminder, that negative mean-removed pressures correspond to a locally thickened portion of the boundary layer, and positive mean-removed pressures to locally thinned portions. The dotted curve in the figure traces out the x-development of an azimuthally thickened portions of the boundary layer. This trajectory should correspond to that of two neighbor stationary cross-flow vortices.

The previous corresponding example of the mean flow distortion produced by the $m = 45$ roughness tip was shown in Figure 11(a). Comparing this with Figure 24(a), we note that besides the smaller azimuthal extent, the locations of the total pressure peaks and valleys are shifted. The reason is that the experiments utilized two different cone tips. Although the roughness dimples were applied in the same manner, it was impossible to guarantee that when the tip was screwed onto the cone frustum, that the dimples would be in the exact same azimuthal location. Comparing the two figures, it appears that the mean flow distortion shifted by approximately 3° with the application of the new cone tip.

The half azimuthal wavelength that would correspond to the $m = 45$ roughness, $\lambda_{45}/2$, is indicated in Figure 24(a). This appears to closely correspond to the spacing between the peak and valley in the azimuthal pressure distribution. This is a good indication the mean flow distortion is the result of the growth of the prescribed stationary cross-flow mode. This is further illustrated by the azimuthal wavenumber spectra of this total pressure distribution shown in Figure 24(b). This shows a predominant peak near $m = 45$. In agreement with the earlier results based on flow visualization (Figure 9) and similar mean total pressure surveys

(Figure 11(b)), the energy in the $m = 45$ mode decays to a minimum near the axial location where the N=10 factor predicted transition to occur.

The effect of the 35 kHz excitation on the spatial development of the mean flow distortion produced by the $m = 45$ roughness tip is shown in Figure 25. Figure 25(a) documents the mean flow distortion. Comparing this to that in Figure 24(a) without 35 kHz excitation indicates some differences. In particular, at the upstream location, the azimuthal variation in the total pressure is smaller, indicating a more uniform boundary layer thickness with less mean distortion. As a reference, $\lambda_{45}/2$ is again indicated in the figure. We note that the wavelength match to $m = 45$ is not as precise as that without the 35 kHz excitation, although that could be the result of the having a weaker mean flow distortion.

The azimuthal wavenumber spectra of the total pressure distribution for the $m = 45$ tip with the 35 kHz excitation is shown in Figure 25(b). This indicates that $m = 45$ is in the band of prominent wavenumbers. However in contrast to the previous case without the 35 kHz excitation, the energy in the $m = 45$ mode decays to a minimum well upstream of the N=10 factor axial location. Thus this indicates that turbulent transition occurred earlier with the addition of the periodic excitation.

As further evidence of the effect of the 35 kHz excitation on the transition location, the method of Schuele et al. [2013] was used to estimate transition location. This involved following the x-trajectory of a minimum in the total pressure distributions in Figures 24(a) and 25(a). The actual trajectories are shown by the dotted curves in those two figures. As previously mentioned, the pressure minima are indicative of a region of local thickening of the boundary layer. Such regions are known to develop an off-wall inflectional shear layer and subsequent inviscid instability that quickly leads to turbulence[Craig and Saric, 2016]. The ending azimuthal locations of both of these trajectories ($138^\circ \leq \theta \leq 140^\circ$)) is where the N-factor=10 curve is furthest upstream on the cone and therefore where transition is expected to occur first.

The x-development of the total pressure along the two pressure minima for the "critical" ($m = 45$) without and with 35 kHz excitation is shown in Figure 26. Normally, estimates of the transition location would involve two approaches. The first, would fit a linear curve to the rise in the total pressure near the wall that would accompany transition, with the x-location where the linear curve intersects a common reference level designating the transition location. However this approach is not possible with the present results because it appears that the rise in the total pressure with the 35 kHz excitation occurred upstream of the most upstream measurements location. Therefore the second approach was used.

The second approach is based on the loss in the coherence of the mean flow distortion. This would be evident as saturation and abrupt decay in the axial development of the total pressure. Based on this approach, shown in red, the addition of the 35 kHz excitation resulted in a 9% decrease in the transition location. Schuele et al. [2013] considered this as an indication of the *late stage* of transition.

As previously mentioned, the total pressure Pitot probes had a frequency response that was capable of detecting the traveling cross-flow modes. Figure 27 shows spectra of off-wall total pressure fluctuations at different azimuthal locations at the most downstream axial location of $x = 16.51$ cm (6.5 in.) for the $m = 45$ roughness tip with and without the

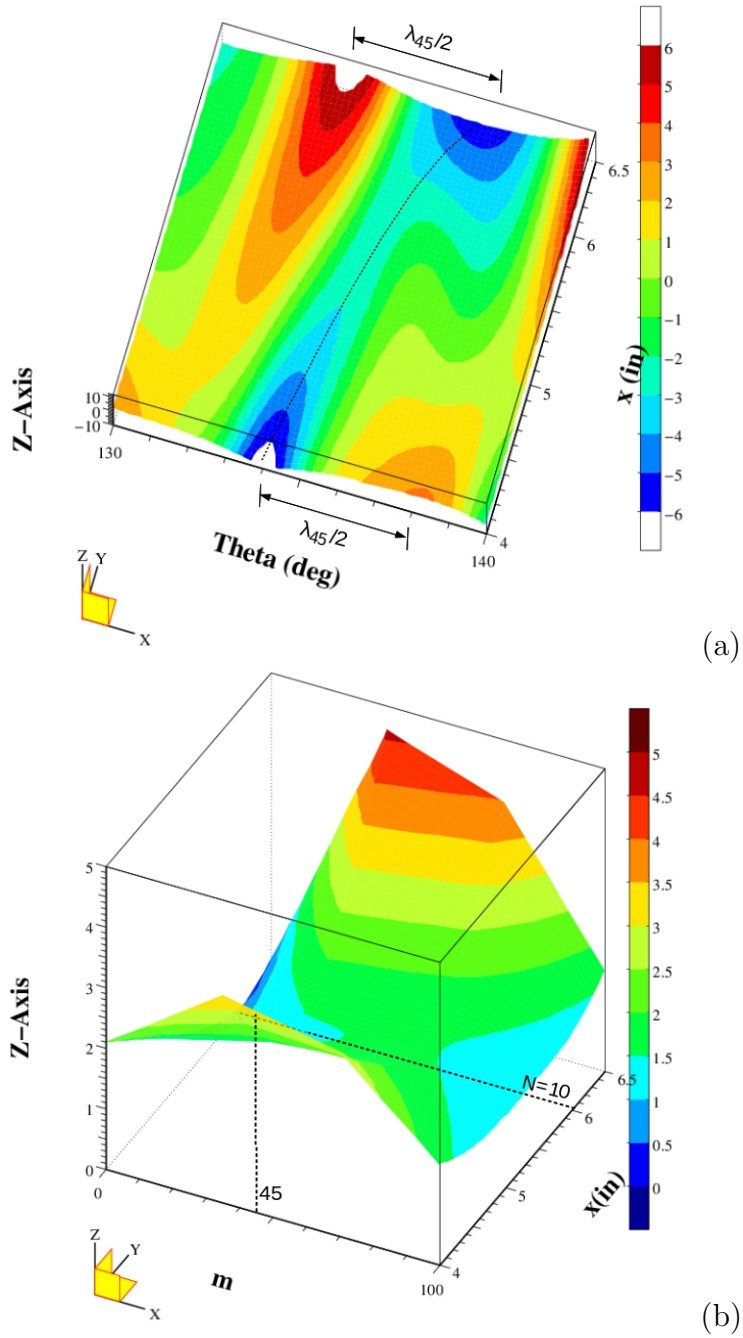

Figure 24: Azimuthal total pressure distributions at a constant height above the surface (a) and corresponding wavenumber spectra (b) for the case with the "critical" ($m = 45$) roughness cone tip without plasma excitation.

35 kHz excitation. As in Figure 23, the dashed curve corresponds to the baseline spectra with the plasma actuator off, and the solid curve corresponds to the spectra with the plasma actuator operating at 35 kHz. The vertical dashed line indicates the 35 kHz frequency in

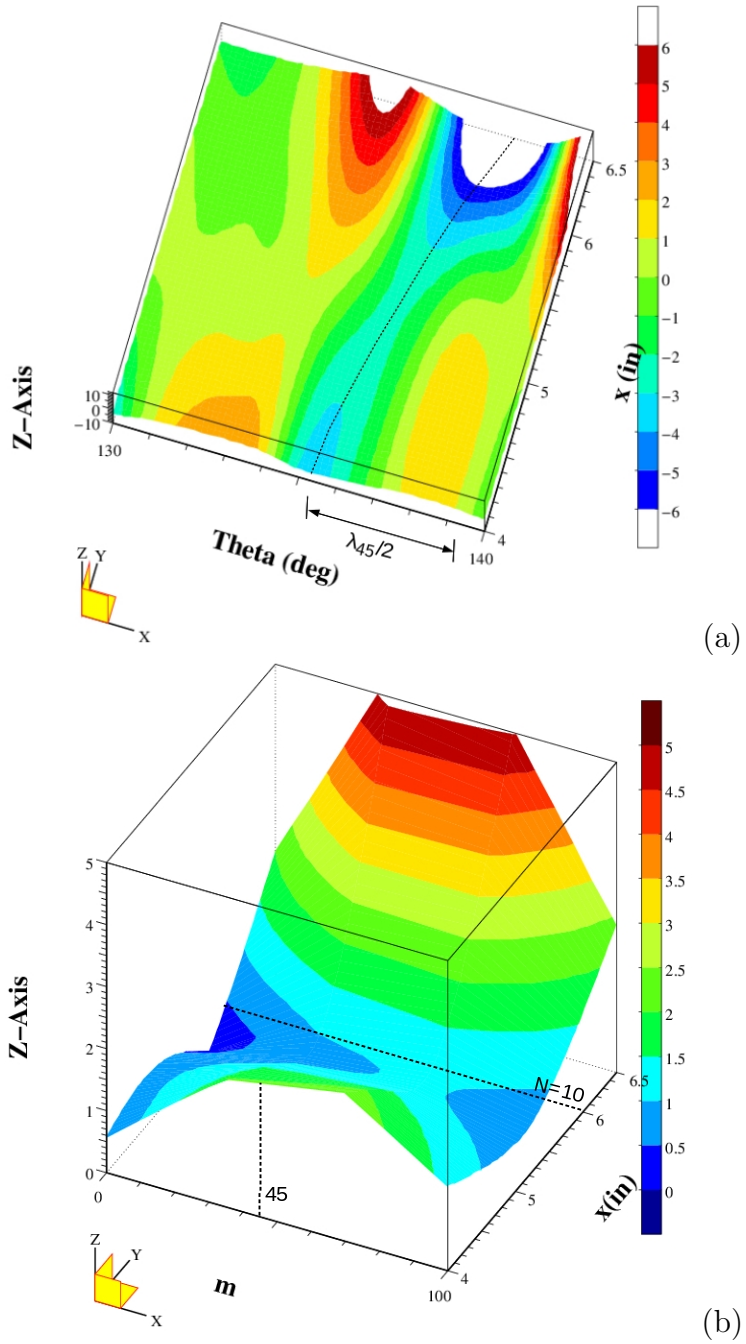

Figure 25: Azimuthal total pressure distributions at a constant height above the surface (a) and corresponding wavenumber spectra (b) for the case with the "critical" ($m = 45$) roughness cone tip with plasma excitation.

the spectra. These spectra indicate that there is an azimuthal variation to the effect of the 35 kHz excitation on the baseline spectra. A similar variation occurred at all of the axial locations.

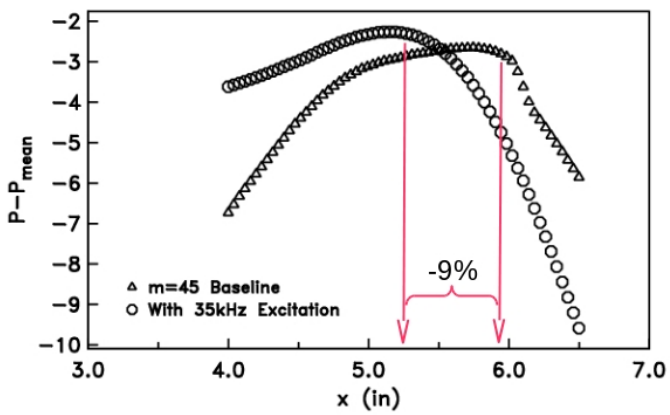

Figure 26: Axial distributions following the pressure minima denoted by the dotted curve in the total pressure distributions in Figures 24 and 25.

To investigate the azimuthal variation in the effect of the 35 kHz excitation, the peak values of the spectra of the traveling disturbances from spectra like those in Figure 27 for all of the measured (θ, x) locations, were used to compile a view of the spatial amplitude distribution for the traveling cross-flow modes. These are shown for the $m = 45$ roughness cone tip without the 35 kHz excitation in Figure 28, and for the same roughness tip with the 35 kHz excitation in Figure 29. Examination of these reveals the presence of features with different azimuthal wavenumbers. As before, to interpret these, one needs to consider possible interactions between the traveling and stationary cross-flow modes.

The underlying assumption of the 35 kHz excitation is that it would impart energy into the band of most amplified traveling cross-flow modes. As observed in the previous results, a nonlinear (quadratic) sum and difference interactions between traveling and stationary cross-flow modes led to observable spatial amplitude distributions in the temporal (traveling) disturbances that could be associated with traveling cross-flow modes.

Utilizing the $m = 45$ roughness tip, Figure 24 documented stationary modes with that azimuthal wavenumber. This mode was designated $(0, 45)$, where the first index is the frequency, and the second is the azimuthal wavenumber. Based on Li et al. [2010], the most amplified traveling cross-flow mode occurs with an azimuthal wavenumber of $m = 40$. The traveling mode is then designated as $(f_t, 40)$, where f_t refers to the frequency of the traveling mode.

The first interaction between these two modes is

$$(0, 45) \pm (f_t, 40) = (f_t, 85) \text{ and } (f_t, 5) \tag{6}$$

where $(f_t, 85)$ and $(f_t, 5)$ are traveling modes with the same frequency as the primary traveling mode. Therefore the amplitude of the spectral peaks in Figure 27 should be representative of not only the primary traveling mode, but also the sum and difference modes that occur at the same frequency.

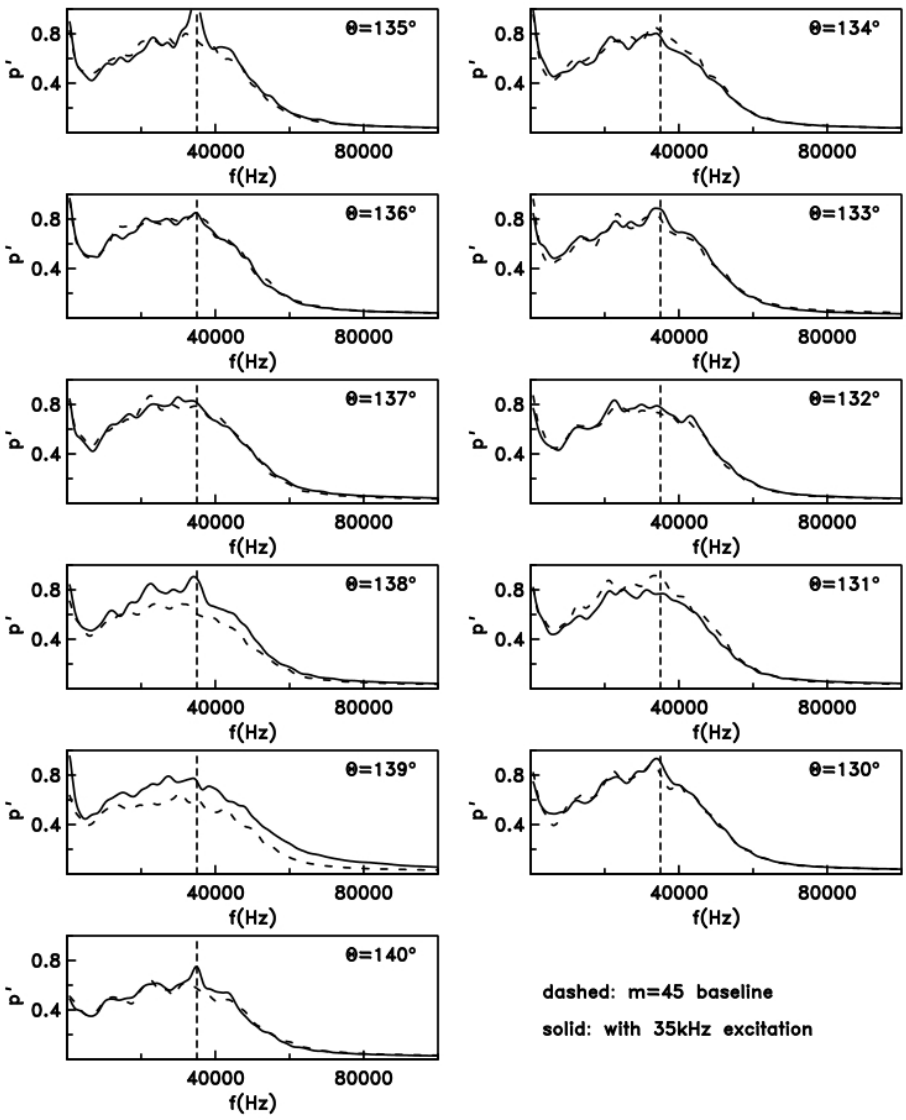

Figure 27: Sample comparison of spectra of traveling disturbances at different azimuthal positions at $x = 16.51$ cm (6.5 in.) with $m = 45$ roughness without and with plasma excitation at 35 kHz.

Now the result of the summing interaction, $(f_t, 85)$, would have an azimuthal wave angle of approximately 4°. That of the difference interaction, $(f_t, 5)$, would have an azimuthal wave angle of 72°. The latter is larger than the azimuthal extent of the measurements. However the former, $(f_t, 85)$, is slightly distinguishable in the spatial amplitude distribution in Figure 28 by the small bump at $\theta = 134°$ at the most upstream x-position.

Also observable is a spatial amplitude distribution with an azimuthal wavenumber that matches that of the discrete roughness, $m = 45$. Because of the limited azimuthal extent, the half wavelength, $\lambda_{45}/2$, is indicated. As previously speculated, this could be due to a

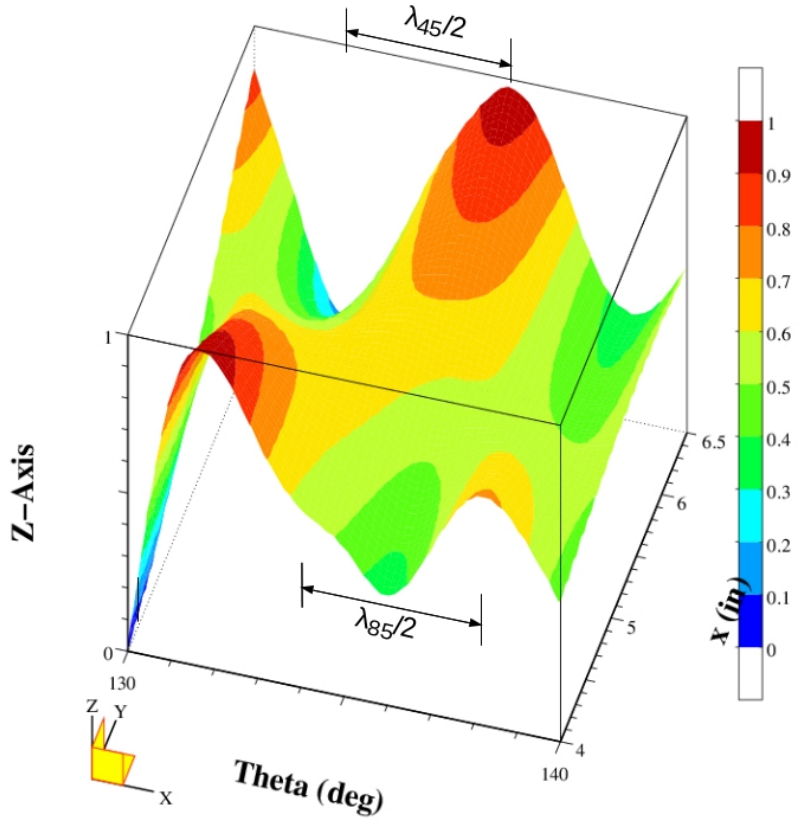

Figure 28: Spatial amplitude distribution of the spectral peak amplitude of the traveling disturbances for the $m = 45$ roughness tip without 35 kHz excitation.

linear superposition that leads to a modulation of the traveling mode amplitude as it rides over the stationary mean flow distortion. An example of such behavior has been identified through Direct Navier Stokes simulations of subsonic 3-D boundary layers undergoing cross-flow instability by Dörr et al. [2017]. However, the cross-bicoherence analysis that follows suggests another explanation.

For the case with the $m = 45$ roughness tip and the 35 kHz excitation, the spatial distribution of traveling disturbances is quantitatively different. In particular, an azimuthal wavelength corresponding to that of the stationary cross-flow mode, $\lambda_{45}/2$, is no longer evident. Instead, there is the strong appearance of the summed mode, $(f_t, 85)$, with azimuthal wavelength λ_{85}, and the primary traveling mode, $(f_t, 40)$, with the half wavelength, $\lambda_{40}/2$, being indicated in the plot. The presence of the latter is a strong indication that the 35 kHz excitation was indeed imparting energy into the most amplified traveling cross-flow mode with an azimuthal wavenumber, $m = 40$.

In order further contrast the differences in the traveling mode spatial amplitude distributions with the 35 kHz excitation, the azimuthal wavenumber spectra of the distributions in Figures 28 and 29 were computed and presented in Figure 30. Figure 30(a) and (b) respectively correspond to the cases without and with the 35 kHz excitation. The most notable

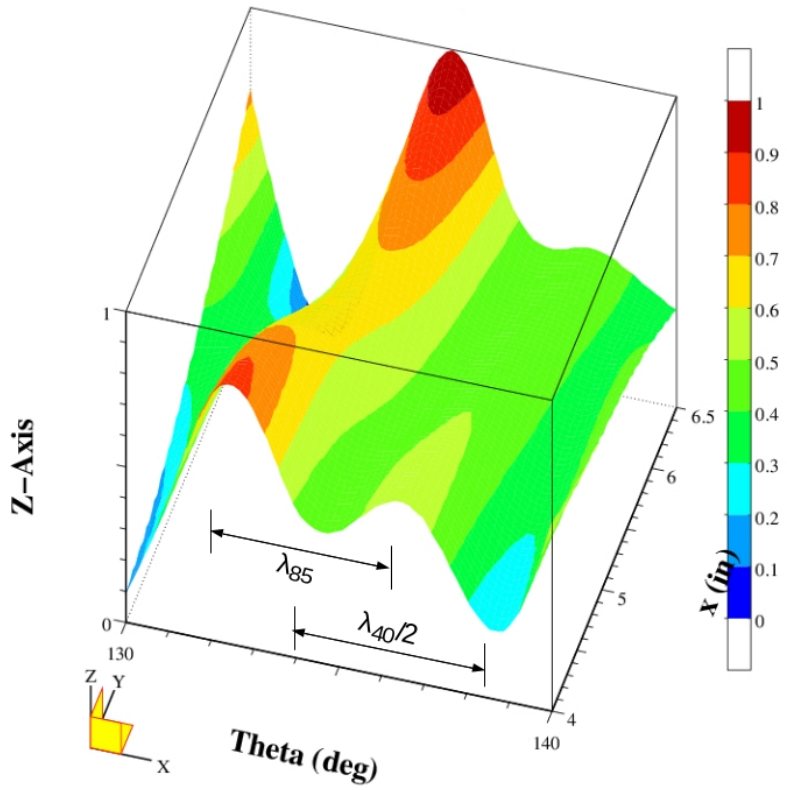

Figure 29: Spatial amplitude distribution of the spectral peak amplitude of the traveling disturbances for the $m = 45$ roughness tip with 35 kHz excitation.

difference between these two is the energy at wavenumbers centered about $m = 85$ that occurs with the 35 kHz excitation that is absent without the excitation.

As was previously done, the cross-bicoherence statistic was used to document the nonlinear interaction between stationary and traveling cross-flow modes. The cross-bicoherence (CBC) is again defined as

$$\beta_{ijk}(m_1, m_2) = \frac{|\tilde{R}_{ijk}(m_1, m_2)|^2}{< |\tilde{p}_i(m_1)|^2 |\tilde{p}_j(m_2)|^2 >< |\tilde{p}_k(m_3)|^2 >} \tag{7}$$

where

$$\tilde{R}_{ijk}(m_1, m_2) =< \tilde{p}_i(m_1)\tilde{p}_j(m_2)\tilde{p}_k^*(m_3) > \tag{8}$$

is the cross-bispectrum, with i, j and k equal to either i or j that refer to one of the two mean-removed pressure time series, p, with azimuthal wavenumbers m_1, m_2 and m_3, respectively. The notation $(||)$ is the modulus of the component, $\sim$ denotes the Fourier transformed function in wavenumber domain, $<>$ represents the ensemble average. These wavenumbers are related to each other such that $m_1 + m_2 + m_3 = 0$.

As before, one of the data series used in the CBC was the azimuthal variation in the time-averaged total pressure, $\bar{p}(\theta)$, at a selected x location on the cone. The same data were

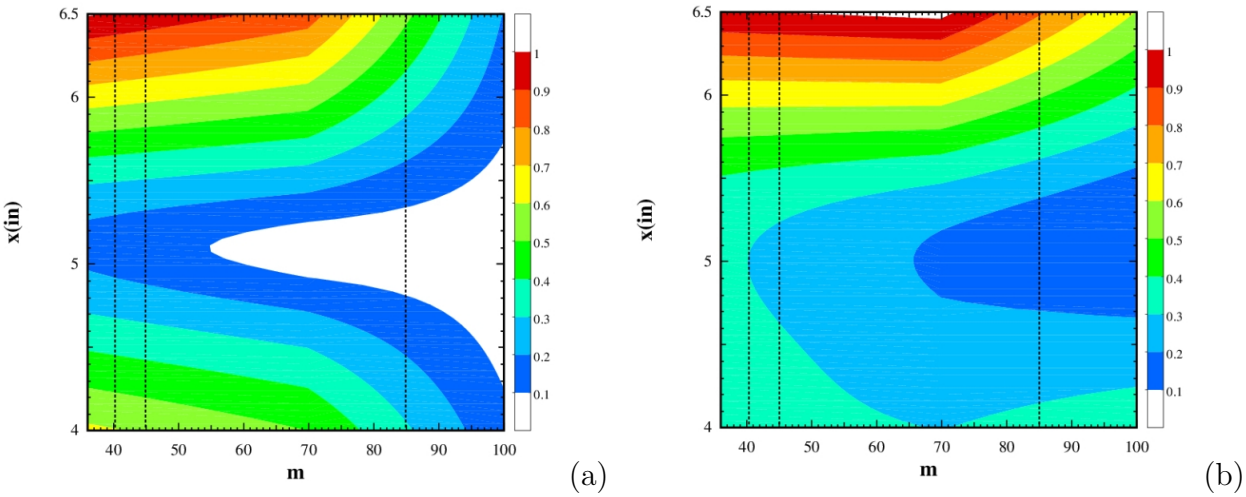

Figure 30: Axial development of the azimuthal wavenumber of the maximum pressure fluctuations of $m = 45$ roughness tip based on Figure 28 with the plasma excitation at 35 kHz off (a) and based on Figure 29 with the plasma excitation at 35 kHz on (b).

used to generate Figures 24(a) and 25(a). This data series therefore represents the azimuthal mean flow distortion at one x location. The Fourier transform of this data series is $\tilde{\bar{p}}(m)$. The wavenumber spectra shown in Figures 24(b) and 25(b) correspond to $|\tilde{\bar{p}}(m)|^2$ at each x location.

The second data series used in the CBC corresponds to the total pressure time series before time averaging, $p(t)(\theta)$, at the same x location as $\bar{p}(\theta)$. This data series contains pressure fluctuations that correspond to the traveling cross-flow modes. The squared modulus of the transformed data series, $|\tilde{p}(f)|^2$, was used to generate the frequency spectra that were shown in Figures 27.

It is necessary that the two transformed data series have the same independent variable units. In $|\tilde{p}(m)|^2$, the independent variable is azimuthal wavenumber, m. In $|\tilde{p}(f)|^2$ the independent variable is frequency, f. Therefore in the case of the latter, we chose to convert frequency to azimuthal wavenumber. As previously pointed out, analysis by Li et al[Li et al., 2010] indicated that the azimuthal wavenumber in the center of the most amplified band of frequencies of traveling cross-flow mode (35 kHz) was $m = 40$. This was used as a point of reference to the conversion from frequency to wavenumber of the traveling mode data series.

Another important step in computing the CBC was that the sampling rates be the same for the two data series. For the time series representing the stationary cross-flow mode, $\bar{p}(\theta)$ (data series 1), the sampling rate was 8.54 pts/$\circ$. For the time series representing the traveling cross-flow mode (data series 2), the sampling rate was considerably less at 0.317 pts/$\circ$. Therefore in order to match the two data sampling rates, data series 2 was zero-padded by the appropriate amount prior to the Fourier transform.

As with linear coherence, the value of the CBC varies between 0 and 1. High values of the CBC indicate a high degree of triple phase locking

$$\theta_i(m_1) + \theta_j(m_2) = \theta_k(m_3) \tag{9}$$

from realization to realization. Here $\theta_i(m_1)$ is the instantaneous circular phase angle of $\tilde{p}_i(m_1)$.

As a reminder, the region of validity of the CBC is set by the Nyquist criterion, where the sum of any two frequencies (or wavenumbers in this case) cannot exceed half the sampling rate. This region then takes the form of two isosceles triangles, one each for sum and difference interactions. This is shown in Figure 31(a) and (b). The region of the CBC where interactions were observed has been enlarged.

For the CBC shown in Figure 31, the data series (1) corresponding to the stationary cross-flow modes is designated by subscript 1, with its wavenumber read from the abscissa. The data series corresponding to the traveling cross-flow modes is designated by subscript 2, with its wavenumber read from the ordinate. The ordinate wavenumbers are either added (top triangle) or subtracted (bottom triangle) from those read on the abscissa to give the third frequency which is read as the intercept of a $-45°$ line to the abscissa. This method for reading the CBC is outlined by the arrows for either the summing interaction or the difference interaction in the two plots.

The decision of which of the two data series (1 or 2) corresponds to the i, j and k series in the calculation of $\beta_{ijk}(m_1, m_2)$ in Equation 7 is important. Based on the results in Figures 28 to 30, that indicate an influence of the stationary cross-flow mode on the spatial amplitude distribution of the traveling cross-flow mode, we chose the order $[i, j, k]$=[1,2,2]. Thus we were investigating an interaction between the stationary mode (1) and the traveling mode (2) that results in sum and difference traveling modes (2).

The CBC statistic involved 256 ensembles. Figure 31(a) corresponds to the $m = 45$ roughness without the 35 kHz excitation. The (x, θ) location corresponds to the most upstream measured location, $x = 10.16$ cm (4 in.), and an azimuthal location ($\theta = 131°$) where the spatial amplitude at the center frequency of the traveling cross-flow mode (35 kHz) was at a peak level as shown in Figure 28. Even without the 35 kHz excitation, the CBC indicates a perfect (CBC=1) triple phase locking between the stationary cross-flow mode generated by the "critical" ($m = 45$) roughness, and the traveling cross-flow mode with azimuthal wavenumber ($m = 40$) to produce a traveling cross-flow mode with an azimuthal wavenumber of $m = 85$. This supports the observation of the weak spatial variation with the λ_{85} azimuthal wavelength in Figure 28.

In contrast to the previous CBC results in Figure 19, the present results indicate a band of difference interactions. A notable one with the highest CBC involves the harmonic wavenumber of the discrete roughness, such that

$$(0, 90) - (f_t, 40) = (f_t, 45). \tag{10}$$

This appears to be the mechanism for the observation of the relatively strong spatial variation with the $\lambda_{45}/2$ azimuthal wavelength in Figure 28. It also points to a powerful mechanism

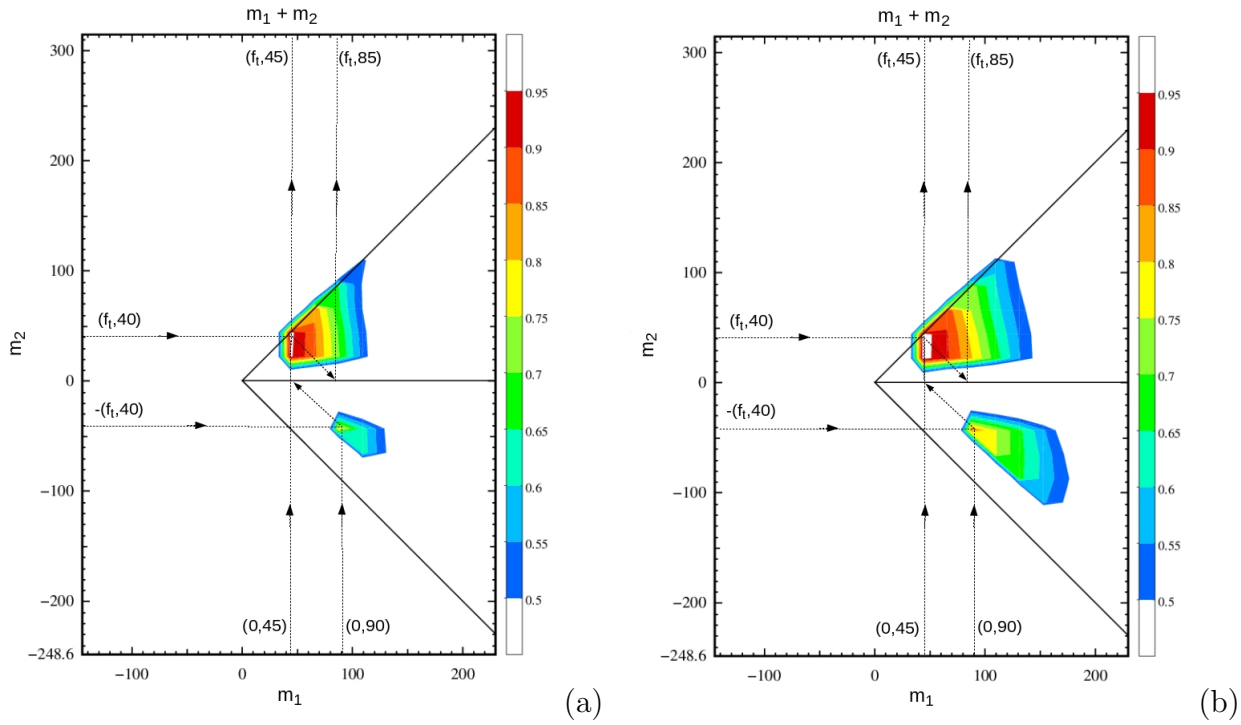

Figure 31: Cross-bicoherence for stationary-traveling-traveling mode interaction at $x = 10.16$ cm (4.0 in.) and $\theta = 135°$ with $m = 45$ roughness tip and plasma excitation at 35 kHz off (a) and on (b).

of spectral broadening in which a band of roughness wavenumbers can lead to a broad band of traveling modes.

The CBC for the case with the $m = 45$ roughness and the 35 kHz excitation is shown in Figure 31(b). The addition of the excitation has enlarged the band of wavenumbers over which a significant triple phase locking exists. The same sum and difference interactions observed for the case without excitation are highlighted. However, the significantly enlarged range of difference interactions could couple a broad spectrum of roughness wavelengths to broad band of traveling modes that hasten transition. This is likely the mechanism by which the 35 kHz excitation moved the transition location upstream in the present experiments.

6 Conclusions

Experiments in the 3-D boundary layer on a right-circular cone at an angle of attack demonstrated the receptivity of stationary cross-flow modes to passive patterned roughness at Mach 6.0. The experiments were performed in a Ludwieg tube that included a conventional nozzle that was not designed to suppress acoustic disturbances. The passive roughness consisted of micron-size indentations (dimples) that were located near the cone tip, just upstream of the first neutral growth branch of stationary cross-flow modes, based on linear stability the-

ory. The roughness dimples encircled the cone tip with a uniform spacing that defined the azimuthal wavenumber of the roughness. Roughness with two different azimuthal wavenumbers were investigated. The first was at a "critical" wavenumber that was approximately centered in the band of the most amplified stationary cross-flow modes. The other was at a"subcritical" wavenumber that was 1.5 times higher than the "critical" wavenumber, and intended to increase the transition Reynolds number. A smooth cone tip representing an uncontrolled baseline was used to substantiate linear theory predictions and to provide contrast to the critical wavenumber roughness case.

The results confirmed that the stationary cross-flow mode was receptive to the passive patterned roughness. Transition front measurements using the Preston tube approach indicated that the transition Reynolds number had increased by 25% with the "subcritical" wavenumber roughness. This compared to a 40% increase in the transition Reynolds number using the same cone model and discrete roughness approach at Mach 3.5 in a "quiet" tunnel by Schuele et al. [2013]. The question remains if this difference is due to the difference in Mach number, or to the free-stream acoustic disturbance level.

The prescribed roughness initial conditions revealed evidence of a nonlinear (quadratic) interaction between the stationary and traveling cross-flow modes. This appeared as an azimuthal variation in the amplitude of the traveling cross-flow mode with azimuthal wavenumbers that corresponded to the sum and difference of the azimuthal wavenumbers of the primary stationary and traveling modes. Cross-bicoherence verified a triple phase locking between the two primary modes and the summed mode for both the "critical" and "subcritical" roughness cases.

The impact that this nonlinear interaction has on transition was expected to depend on the initial amplitude of the traveling modes. Therefore, follow-on experiments were performed in which a plasma actuator ring on the cone tip, placed just downstream of the azimuthal array of discrete roughness, was used to control (enhance) the amplitude of the most amplified traveling cross-flow mode. The excitation was at 35kHz which was predicted and verified in the experiments, to be in the center of the band of most amplified traveling cross-flow modes. Our objective was to provide controlled excitation whose amplitude was low enough to *prevent* a bypass the linear development of the traveling cross-flow modes. We believe this was accomplished.

Spectra of total pressure fluctuations taken above the cone surface at different azimuthal and axial locations verified the receptivity of the boundary layer to the 35 kHz excitation. This affected the azimuthal and streamwise development of the stationary cross-flow modes. The general effect was to move the transition location upstream by 9%.

The nonlinear (quadratic) interaction between the stationary and traveling cross-flow modes was further enhanced by the excitation of the traveling cross-flow mode. This was particularly evident by the enlarged band of wavenumbers over which a significant triple phase locking existed. In particular the significantly enlarged range of difference interactions could couple a broad spectrum of surface roughness wavelengths to a broad band of traveling modes that could hasten transition. This is likely the mechanism by which the 35 kHz excitation moved the transition location upstream in the present experiments. It also provides an explanation for lower transition Reynolds number observed in conventional

tunnels compared to those in quiet tunnels and in flight.

The controlled traveling cross-flow mode experiments were preformed with the "critical", $m = 45$, cone tip roughness. Future experiments should also investigate the effect of higher traveling mode disturbance levels on the "sub-critical" roughness that is designed to suppress transition. This would answer the original motivation to explain the apparent reduced transition suppression effectiveness that was exhibited in these experiments in the high disturbance conventional tunnel.

7 Archival publications during this period:

1. Control of Stationary Cross-flow Modes in a Mach 6 Boundary Layer Using Patterned Roughness. T. Corke, A. Arndt, E. Matlis and M. Semper, *J. Fluid Mech.*, **856**, 2018, 822-849.

2. Hypersonic Boundary Layer Cross Flow Transition - Characteristics and Control. T. Corke, A.. Arndt, E. Matlis, R. Bowersox and I. Neel, To appear *AIAA J. Spacecraft and Rockets*, 2019.

3. Chapter 12: Hypersonic Boundary Layer Cross Flow Transition - Characteristics and Control. T. Corke, A.. Arndt, E. Matlis, R. Bowersox and I. Neel, Chapter 12, *Final Report - NATO AVT-240 Working Group on Hypersonic Boundary Layer Transition*, 2018.

8 Changes in research objectives:

None

9 Change in AFOSR program manager:

No

10 Extensions granted:

Yes

11 Discoveries, inventions, or patent disclosures:

The key discovery was a quantitative confirmation of the quadratic phase locking between the initial stationary and traveling cross-flow modes and their sum and difference modes that were previously brought out by spatial amplitude distributions. The Year 3 experiments determined the receptivity of traveling cross-flow modes to surface plasma actuator excitation. When excited at the most amplified traveling cross-flow mode frequency, it produced quantifiable changes in the stationary cross-flow mode that reduced the transition location by 9%.

References

C-Y Schuele, T. Corke, and E. Matlis. Control of Stationary Cross-flow Modes in a Mach 3.5 Boundary Layer Using Patterned Passive and Active Roughness. *J. Fluid Mech.*, 718: 5–38, 2013.

M. V. Morkovin. Panel summary on roughness. Instability and Transition, Vol. I, Springer-Verlag, 1990a.

M. V. Morkovin. On roughness-induced transition: Facts, views & speculation. Instability and Transition, Vol. I, Springer-Verlag, 1990b.

E. Reshotko. Paths to Taransition Wall Layers. Papers presented during the AVT-151 RTO AVT/VKI Lecture Series held at the von Karman Institute, Rhode St. Gen, Belgium., 09-12 June 2008.

W.S. Saric, H.L. Reed, and E.J. Kerschen. Boundary-Layer Receptivity to Freestream Disturbances. *Annual Review of Fluid Mechanics*, 34:291–319, 2002.

H. Bippes. Basic Experiments on Transition in Three-dimensional Bboundary Layers dominated by crossflow instability. *Progress in Aerospace Sciences*, 35:363–412, 1999.

M. Malik, F. Li, and C.-L. Chang. Crossflow disturbances in three-dimensional boundary layers: nonlinear development, wave interaction and secondary instability. *J. Fluid Mech.*, 268:1–36, 1994.

M. Malik, F. Li, M. Choudhari, and C.-L. Chang. Secondary instability of crossflow vortices and swept-wing boundary-layer transition. *J. Fluid Mech.*, 399:85–115, 1999.

Valery G. Chernoray, Alexander V. Dovgal, Victor V. Kozlov, and Lennart Loefdahl. Experiments on Secondary Instability of Streamwise Vortices in a Swept-Wing Boundary Layer. *Journal of FLuid Mechanics*, 534:295–325, 2005.

E. B. White and W. S. Saric. Secondary Instability of Crossflow Vortices. *Journal of Fluid Mechanics*, 525:275–308, 2005.

W.S. Saric, H.L. Reed, and E.B. White. Stability and Transition of Three-Dimensional Boundary Layers. *Annual Review of Fluid Mechanics*, 35:413–440, 2003.

H. L. Reed and W. S. Saric. Stability of Three-Dimensional Boundary Layers. *Annual Review of Fluid Mechanics*, 21:235–284, 1989.

P. Wassermann and M. Kloker. Mechanisms and passive control of crossflow-vortex-induced transition in three-dimensional boundary layer. *J. Fluid Mech.*, 456:49–84, 2002.

G. Bonfigli and M. Kloker. Secondary instability of crossflow vortices: validation of the stability theory by direct numerical simulation. *J. Fluid Mech.*, 583:229–272, 2007.

S. Craig and W. Saric. Crossflow instability in a hypersonic boundary layer. *J. Fluid Mech.*, 808:224–244, 2016.

T. C. Corke and K. F. Knasiak. Stationary Travelling Cross-Flow Mode Interactions on a Rotating Disk. *Journal of Fluid Mechanics*, 355:285–315, 1998a.

T. Corke, E. Matlis, and H. Othman. Transition to turbulence in rotating-disk boundary layers - convective and absolute instabilities. *J. Engr. Math.*, 57:253–272, 2007.

William S. Saric, Carillo Ruben C, and Mark S. Reibert. Leading-Edge Roughness as a Transition Control Mechanism. AIAA Paper AIAA-98-0781, 1998.

R.H. Radeztsky Jr., M.S. Reibert, and W.S. Saric. Effect of Isolated Micron-Sized Roughness on Transition in Swept-Wing Flows. *AIAA Journal*, 37(11):1370–1377, 1999.

W. S. Saric and H. L. Reed. Supersonic Laminar Flow Control on Swept Wings Using Distributed Roughness. AIAA Paper AIAA 2002-0147, 2002.

W.S. Saric, H.L. Reed, and D.W. Banks. Flight Testing of Laminar Flow Control in High-Speed Boundary Layers. Paper presented at the RTO AVT Specialists' Meeting on 'Enhancement of NATO Military Flight Vehicle Performance by Managemenet of Interacting Boundary Layer Transition and Separation', held in Prague, Czech Republic , 4-7 October 2004, Published in RTO-MP-AVT-111, 2004.

N.V. Semionov and A.D. Kosinov. Method Laminar-Turbulent Transition Control of Supersonic Boundary Layer on a swept Wing. *Thermophysics and Aeromechanics*, 14(3): 337–341, 2007.

N.V. Semionov, A.D. Kosinov, and V.Ya. Levchenko. Experimental Study of Turbulence Beginning and Transition Control in a Supersonic Boundary Layer on Swept Wing. R. Govindarajan (ed.), Sixth IUTAM Symposium on Laminar Turbulent Transition, 2006.

R.A. King. Three-Dimensional Boundary-Layer Transition on a Cone at Mach 3.5. *Experiments in Fluids*, 13:305–314, 1992.

Stephen W.D. Wolf and James A. Laub. NASA Ames Laminar Flow Supersonic WInd Tunnel (LFSWT) Tests of a 10° Cone at Mach 1.6. NASA-TM 110438, 1997.

M. Estorf, T. Wolf, and R. Radespiel. Experimental and numerical investigations on the operation of the Hypersonic Ludwieg Tube Braunschweig. 5th European Symposium on Aerothermodynamics for Space Vehicles, 2004.

R. Cummings and T. McLaughlin. Hypersonic Ludwieg tube design and future usage at the U.S. Air Force Academy. 50th AIAA Aerospace Sciences Meeting, Paper AIAA 2012-0734, 2012.

C-Y Schuele. Control of stationary cross-flow modes in a Mach 3.5 boundary layer using passive and active roughness. Ph.D. Thesis, University of Notre Dame, Notre Dame, IN, 2011.

F. Li, M. Choudhari, C-L Chang, and J. White. Analysis of instabilities in non-axisymmetric hypersonic boundary layers over cones. 10th AIAA/ASME Joint Thermophysics and Heat Transfer Conference, Paper AIAA 2010-4643, 2010.

E. Swanson and S. Schneider. Boundary-layer transition on cones at angle of attack in a Mach-6 quiet tunnel. 48th AIAA Aerosciences Meeting, Paper AIAA Paper 2010-1062, 2010.

W. S. Saric. Private Communication, 2008.

M. S. Reibert. Nonlinear Stability, Saturation, and Transition in Crossflow-Dominated Boundary Layers. Ph.D. Thesis, Arizona State University, 1996.

M. Glauser, W. Saric, K. Chapman, and M. Reibert. Swept-wing boundary layer transition and turbulent flow physics from multipoint measurements. *AIAA Journal*, 52(2):338–347, 2014.

T. Corke and K. Knasiak. Stationary-traveling cross-flow mode interactions on a rotating disktransition to turbulence in rotating-disk. *J. Fluid Mech.*, 355:285–315, 1998b.

T. Corke and E. Matlis. Transition to turbulence in 3-d boundary layers on a rotating disk (triad resonance). One Hundred Years of Boundary Layer Research, Springer SMIA Book Series, Vol. 129, 2006.

P. Dörr, M. Kloker, and A. Hanifi. Effect of upstream flow deformation using plasma actuators on crossflow transition induced by unsteady vortical free-stream disturbances. 47th AIAA Fluid Dynamics Conference, Paper AIAA 2017-3114, 2017.

I. T. Neel, A. Leidy, N. R. Tichenor, and R. D. Bowersox. Influence of environmental disturbances on hypersonic crossflow instability on the hifire-5 elliptic cone. In *Presnted at AIAA Scitech 2018, paper number to be assigned*. American Institute of Aeronautics and Astronautics, January 2018.

Thomas Juliano and Steven Schneider. Instability and Transition on the HIFiRE-5 in a Mach-6 Quiet Tunnel. *40th Fluid Dynamics Conference and Exhibit*, (July):1–34, 2010. doi: 10.2514/6.2010-5004.